

Nikola Šimić, BSc

High Resolution STEM Simulation of Beryl Crystal Impurities using Multislice Methods (QSTEM)

MASTER'S THESIS

to achieve the university degree of
Diplom-Ingenieur
Master's degree programme: Technical Physics

submitted to

Graz University of Technology

Supervisor

Ferdinand Hofer, Ao.Univ.-Prof. Dipl.-Ing. Dr.techn.

Co-Supervisor

Daniel Knez, Dipl.-Ing. Dr.techn.
Institute for Electron Microscopy and Nanoanalytics

AFFIDAVIT

I declare that I have authored this thesis independently, that I have not used other than the declared sources/resources, and that I have explicitly indicated all material which has been quoted either literally or by content from the sources used. The text document uploaded to TUGRAZonline is identical to the present master's thesis.

Date, Signature

Abstract

The development of Scanning Transmission Electron Microscopy (STEM) has enabled measuring and analyzing many kinds of materials with atomic resolution either via direct imaging or spectral analysis. These methods are especially interesting in the field of materials science, where crystal or material defects can be resolved directly thanks to the atomic resolution. This possibility is exploited in the analysis of the Beryl-Crystal $\text{Al}_2\text{Be}_3[\text{Si}_6\text{O}_{18}]$, where empty channels are formed due to the crystals hexagonal structure. High-Resolution STEM images of these empty channels have shown significant contrast values within these channels. This thesis covers the simulation of STEM imaging using the multislice method via QSTEM to prove that the channels are filled with foreign atoms and to make an attempt of determining which elements are located in the channels. Different approaches of evaluating simulation data are shown, as well as a clear documentation for future users on how to replicate the results.

Kurzfassung

Die Entwicklung der Rastertransmissionselektronenmikroskopie (auf englisch STEM) hat es ermöglicht eine Vielzahl von Materialien entweder durch direkte bildgebende Verfahren oder durch spektroskopische Methoden mit atomarer Auflösung zu analysieren. Diese Methoden haben eine besonders große Bedeutung in den Materialwissenschaften, wo Kristall- und Materialdefekte dank der atomaren Auflösung dargestellt werden können. Dies wird in der Analyse des Beryllkristalls $\text{Al}_2\text{Be}_3[\text{Si}_6\text{O}_{18}]$ ausgenutzt, wo in der hexagonalen Kristallstruktur leere Kanäle vorliegen. Hochauflösungs-STEM Bilder dieses Kristalles haben signifikante Kontrastwerte innerhalb dieser Kanäle gezeigt. Diese Arbeit widmet sich der Simulation hochaufgelöster STEM Bilder durch die Multislice-Methode mit dem Programm QSTEM um zu zeigen, welche Fremdatome sich in den Kanälen anlagern. Es werden weiters verschiedene Ansätze zur Auswertung der Simulationsdaten gezeigt, mitsamt einer detaillierten Dokumentation für zukünftige Simulationen.

Contents

1	Introduction	8
2	Fundamentals	9
2.1	Terminology	9
2.2	The Beryl Crystal	9
3	The Multislice-Method	10
3.1	Theory	10
3.2	QSTEM	11
3.3	Preparing Crystal Models	11
3.3.1	VESTA	11
3.3.2	QSTEM - convert2cfg	13
4	Performing Simulations	14
4.1	Investigating TDS Run Influence	16
5	Simulation Results	18
5.1	One Cs-Dopant	19
5.2	One K-Dopant	24
5.3	One Na-Dopant	27
5.4	Five Na-Dopants	29
5.5	66 Na-Dopants	31
6	Data Evaluation and Interpretation	32
6.1	One Cs-Dopant	33
6.2	One K-Dopant	35
6.3	One Na-dopant	37
6.4	Five Na-Dopants	39
6.5	66 Na-Dopants	41
7	Evaluating Experimental Data	43
8	Summary	48
	Appendices	49
A	MATLAB Code	49
	References	54

1 Introduction

The mineral beryl can be found worldwide, mostly in granites and granite pegmatites. Beryl is not only an important source for beryllium, with crystal in different colors it is also a highly valuable gemstone for jewelry.

The crystal is ideally composed of $\text{Al}_2\text{Be}_3[\text{Si}_6\text{O}_{18}]$, although this formula can change due to doping with foreign atoms.

Beryl is a ring silicate with a special property. Due to octahedral coordination of aluminum ions and tetrahedral coordination of beryllium and silicon ions a crystal channel with a diameter of ≈ 0.5 nm is formed.

The crystal structure of beryl was already analyzed in 1926 with X-ray diffraction methods [1] and refined in many subsequent research papers. Many research groups have been doing research on the crystal chemistry of beryl for 50 years [2], which has shown two special properties: Low concentrations of Cr, V, Mn, Fe or other elements can change the color of the crystal, thus creating the known gems such as emerald, heliodor and aquamarine. However, the crystal channels can also be filled with alkaline metals such as Na, K or Cs, but also with molecules like H_2O or CO_2 . These elements occur in very low concentrations, down to the ppm range.

Recent research has focused on the physical properties of the molecules within the crystal channels. It was shown that water molecules within the channels have ferroelectric properties [3] and also exhibit quantum tunneling behavior [4].

While macroscopic properties of the beryl crystal are already well understood there is only little research on the microscopic crystal structure. Although HR-TEM methods are excellent for such research the feasibility of these methods is reduced to nil by the fact that high energy electrons completely destroy the crystal structure within seconds. There are only few successful TEM experiments of beryl due to beam damage limitations.

The beryl structure was successfully investigated at Graz University of Technology with a resolution of ≈ 0.25 nm in 1990 [5]. Atomic resolution was not yet achievable due to technical limitations, but the ASTEM-Microscope at the FELMI-ZFE made it possible to measure the crystal structure with atomic resolution [6]. A Norwegian group published similar research shortly afterwards [7].

The research group at FELMI-ZFE has focused on the analysis of molecules and ions within the crystal channels of various beryl crystals like emerald, aquamarine and goshenite in recent years. For this the ASTEM microscope with a special cathode and aberration correction, especially spherical aberration, proved invaluable [8]. This research has led to the realization that the experimental results need to be supported with theoretical images of High Angle Annular Dark Field (HAADF) detectors in order to make interpretation of results easier.

2 Fundamentals

This section covers the basic terminology used in this thesis as well as the general assumptions and parameters for the simulations. In addition, the crystal beryl and some of its properties are shown alongside the methods of creating and modifying existing digital crystal model files. Finally, the importance of precise simulation input file preparation is explained, as minor inconsistencies in the files may have great impact on simulation performance.

2.1 Terminology

- FEI HAADF detector - High Angle Annular Dark Field detector by the company FEI
- Gatan HAADF detector - High Angle Annular Dark Field detector by the company Gatan
- Gatan ABF detector - Annular Bright Field detector by the company Gatan
- TDS - Thermal Diffusive Scattering
- QSTEM - Quantitative STEM, a program which allows simulation of (S)TEM images. [9]

2.2 The Beryl Crystal

The beryl crystal forms a hexagonal structure, it belongs to the $P6/mcc$ space group. The model used for the beryl crystal is shown in figure 1.

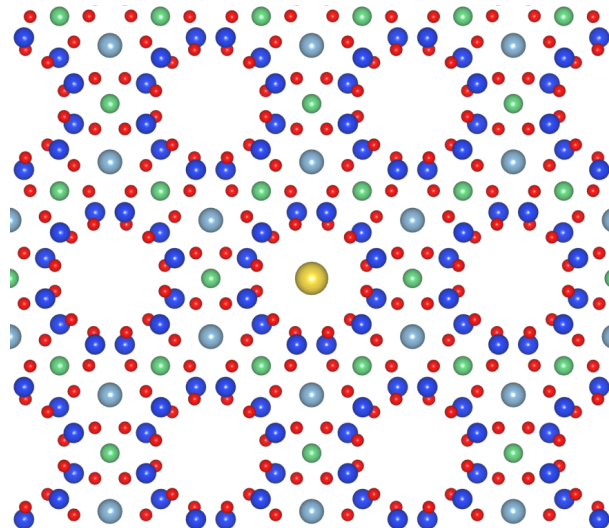


Figure 1: Beryl crystal as seen from the c -direction. A foreign atom is shown in the center channel for illustration purposes. The atoms are marked by colors, with red being oxygen, dark blue silicon, light blue aluminium, green beryllium.

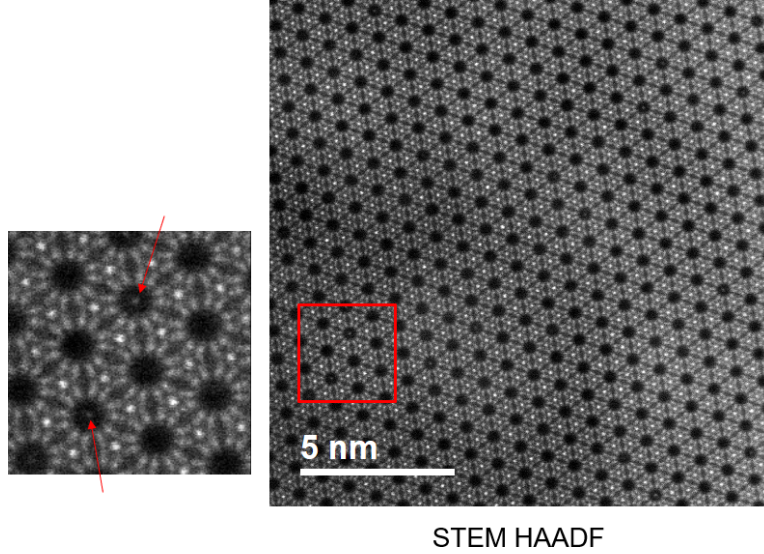


Figure 2: ASTEM HAADF image of bluegreen aquamarine, Christian Gspan (February 2015). Bright regions are clearly visible in the center of empty crystal channels.

As seen in figure 1, the channels formed by Si- and O rings with a size of $d \approx 0.5$ nm [10] are large enough to fit foreign atoms. This fact, as well as the observation of contrast values inside the channels in real HR-STEM measurements (see figure 2) has led to the necessity of simulations, in order to verify the existence of foreign atoms inside the channels as well as make an attempt of categorizing the dopants.

3 The Multislice-Method

The multislice method is a technique used for calculating elastic electron scattering potentials and beam interaction based on model data. The total crystal scattering potential is divided into slices. The simulated electron beam is scattered at each potential slice site and is propagated further through the material. The following section will cover a brief illustration of the mathematical model which is the basis for simulations.

3.1 Theory

The following description is adapted from the dissertation thesis by C. T. Koch (2002) [11]

The main assumptions made are the modulated plane wave approximation

$$\Psi(\vec{r}) = e^{2\pi i \vec{k} \cdot \vec{r}} \Phi(\vec{r})$$

and the high energy approximation $k_z \gg |\vec{g}| \implies \frac{\partial^2 \Phi(\vec{r})}{\partial z^2} \ll 4\pi i k_z \frac{\partial \Phi(\vec{r})}{\partial z}$ (with \vec{g} being the reciprocal lattice vector).

This leads to a modified Schrödinger equation:

$$\frac{\partial \Phi(\vec{r})}{\partial z} = \left(\frac{i \nabla_t^2}{4\pi k_z} - \frac{\vec{k}_t}{k_z} \cdot \nabla_t \right) \Phi(\vec{r}) + \frac{2m|e|i}{4\pi k_z \hbar^2} V(\vec{r}) \Phi(\vec{r})$$

where the gradient of $\Phi(\vec{r})$ disappears if the condition $\vec{k}_t = 0$ is set, which leads to

$$\frac{\partial \Phi(\vec{r})}{\partial z} = \frac{i \nabla_t^2}{4\pi k_z} \Phi(\vec{r}) + \frac{2m|e|i}{4\pi k_z \hbar^2} V(\vec{r}) \Phi(\vec{r})$$

Since this is a linear first order differential equation in z , the equation can be solved by numerical integration via slicing of the potential parallel to the crystal surface. The wave function $\Phi(\vec{r})$ is then represented as a function of the crystal thickness t and the potential slice thickness Δt . The potential is reduced to a 2D function, as each potential slice is integrated along t .

3.2 QSTEM

QSTEM is one of many programs that can be used for simulating TEM and STEM images written by C. T. Koch at the Arizona State University. It utilizes the multislice method, as described above. QSTEM's advantages lie in the intuitive graphical user interface, as well as the variable detector settings. Furthermore, with enough computational power and memory, there is no limit to the number or complexity of simulations performable at the same time.

Using QSTEM efficiently requires the knowledge of generating crystal model data and microscope parameters, as consistent use of input data is most important for creating replicable simulation results. The following list contains all parameters used for the simulations entailed within this thesis, unless explicitly stated otherwise.

3.3 Preparing Crystal Models

Before initiating simulations in QSTEM one needs to prepare the data of the crystal to be simulated. The fastest way of creating crystal models is to obtain crystallographic unit cell data on one of various databases (the Crystallography Open Database [12–17] for instance). One can then either edit the crystal files manually with a generic text editor or resort to 3D visualization software like VESTA [18]. This section will cover a short introduction and tutorial on how to create crystal models from unit cell data using VESTA.

3.3.1 VESTA

Figure 3 shows the beryl unit cell retrieved from the Crystallography Open Database. Crystal models of various file formats are supported with VESTA, which include, among many others, .xyz, .xtl and .cif. For the purposes of simulation STEM images the most interesting of those formats are the .vesta and .xyz formats, as these allow simple manipulation of crystals and transformation to QSTEM configuration files (.cfg) respectively.

In order to create a bulk crystal from unit cell data one needs to replicate the unit cell until the model reaches its required size. This can be easily done by opening the "Objects" sub-menu and choosing the "Boundary" option. One can then proceed to enter the desired range of fractional coordinates, applying the settings will update the crystal size. Notice however, that this procedure only works with crystal data that contains information on the unit cell, as

replication of the unit cell would not be possible otherwise (such is the case with .xyz files, for instance).

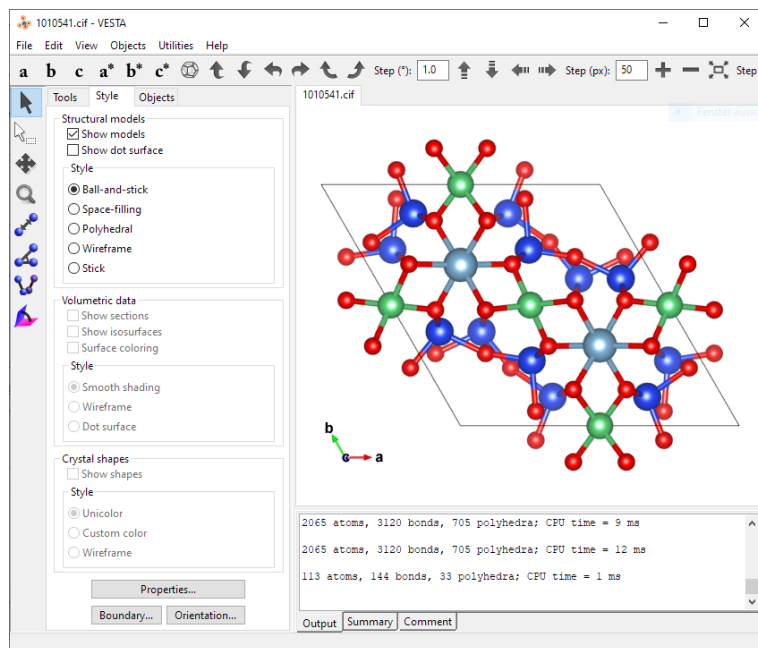


Figure 3: User Interface of VESTA with the unit cell of beryl. The graphical user interface allows for intuitive manipulation of the crystal.

Once the desired size is set, one can add foreign atoms to the crystal. For this there are several options available. The unit cell itself can be manipulated by using the "Edit Data" option in the "Edit" sub-menu, where crystal symmetry options and structure parameters are selectable, as shown in figures 4 and 5. Adding atoms in .vesta and .cif files containing unit cell information will adjust the unit cell accordingly, which means that the foreign atom will be replicated alongside the unit cell across the crystal bulk.

To prevent adding atoms across the whole bulk sample one should first save the replicated bulk crystal data via the "Export Data" option in the "File" sub-menu and save the crystal as a .xyz file. This file type does not contain any crystal symmetry information, as such its size cannot be varied by using VESTA alone.

Furthermore, adding atoms to the crystal will only add one single atom at the desired location. Creating crystals with realistic thickness values (about 30 nm) requires a replication of about $6 \times 6 \times 33$ unit cells in x -, y - and z - direction respectively.

Crystals of this size will result in VESTA loading about 70000 objects on screen, which is a challenge even for modern computer systems. Atoms are still placeable with any text editor, however. In order to do this, one needs to create a .xyz file with the crystal in desired size and open it with an editor afterwards. Keep in mind however, that the first line must be adapted to fit the new number of atoms. The exact formatting of the file must be kept as well, since the QSTEM sub-program convert2cfg requires very specific formatting for .xyz files.

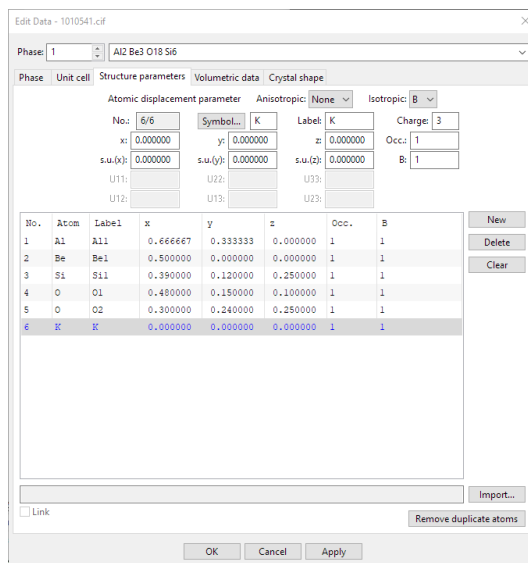


Figure 4: VESTA sub-menu for editing crystal data. Depending on the file format, the whole crystal bulk or only individual atoms are modified.

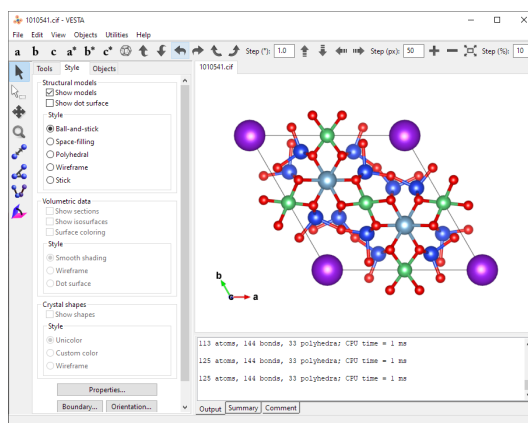


Figure 5: Beryl unit cell with K (purple spheres) added at the channel sites. Adding an atom at the unit cell coordinates $[000]$ adds it at equivalent sites across the whole crystal.

3.3.2 QSTEM - convert2cfg

The program `convert2cfg` contained within the software package of QSTEM creates `.cfg` files from `.xyz` files. The `.cfg` format is used as model file by QSTEM.

While executing the program and converting `.xyz` files to `.cfg` is easy enough, one should know that the `.xyz` formatting required by `convert2cfg` is not the same as the one given by exporting data with VESTA.

The column containing atomic names has two allocated character spaces, which means that atoms with only one character can either be aligned on the left or right side. Files exported by VESTA align one character atom names on the right side, while `convert2cfg` expects the names to be aligned on the left side. A discrepancy will result in conversion failure. Since manual correction of thousands of lines is very tedious and time consuming, a simple

program was written to take .xyz files and shift single character atom names to the "correct" position. The code is shown in the appendix

4 Performing Simulations

This section will cover how simulations were performed (after creating the necessary input files). A simulation example will be shown alongside the input data used in figure 7.

The input data are shown in the following list. These values are used in all simulations, unless explicitly stated otherwise. The parameters, their effect on simulation results and the reasoning behind their choice are explained afterwards.

- **Scan window size X/Y:** [28 to 53 Å / 12 to 37 Å]
- **Scan window resolution:** 200 × 200 pixels
- **Probe array size:** 400 × 400 pixels
- **Probe array resolution:** 0.0265 Å × 0.0265 Å
- **Probe array window size:** 10.6 × 10.6 Å
- **Number of horizontal sub slabs:** 1
- **Number of slices per sub slab:** 99 for crystal thickness of 11 unit cells, 297 for crystal thickness of 33 unit cells
- **Slice thickness:** 1.0219 Å
- **Potential offset X/Y/Z:** 0 Å / 0 Å / 0.511 Å
- **High Voltage:** 300 kV
- **Defocus:** 0 nm
- **Astigmatism:** 0 nm
- **Spherical Aberration:** 0 nm
- **Temperature:** 300 K
- **TDS runs:** 5
- **Cc:** 1 mm
- **dE:** 0.6 eV
- **Convergence angle:** 15 mrad
- **Beam tilt X/Y:** [0°, 0°]
- **Brightness:** $5 \cdot 10^8 \frac{\text{A}}{\text{cm}^2\text{sr}}$
- **Dwell time:** 1 μs

The scan window size is chosen as such to cover the filled channel and six surrounding empty channels, while the resolution is set to 200 × 200 pixels in order to achieve high image quality with acceptable simulation duration.

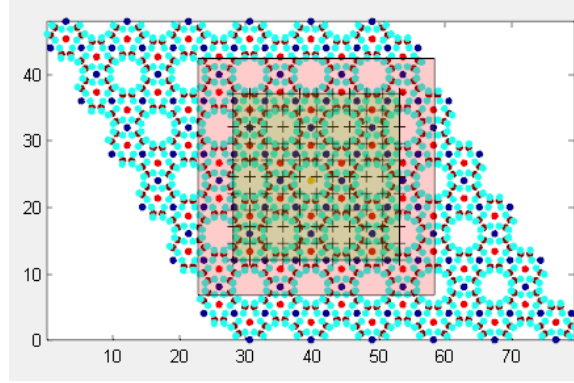


Figure 6: Simulation setup of beryl crystal with Na and O filled column, view from the c-direction.

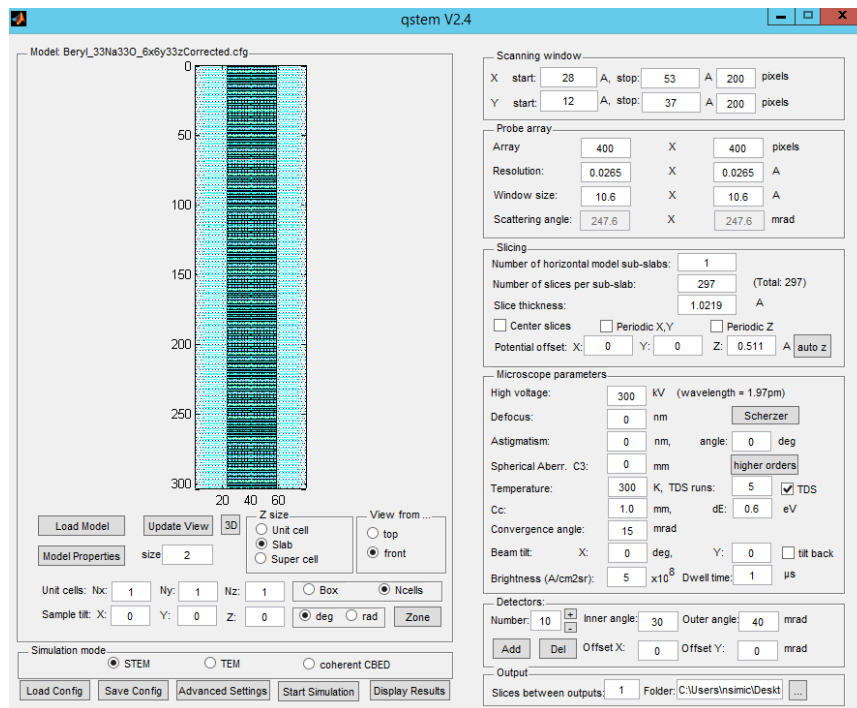


Figure 7: Simulation setup of beryl crystal with Na and O filled column. The preview window to the upper left shows the beryl crystal from the y-direction. Detector angle ranges are listed separately.

The probe array parameters determine which volume of the crystal will be used for scattering potential calculation. The area is denoted as light red area in figures 6 and 7. These parameters also determine the maximum possible scattering angle. This value must be at least the size of the highest detector collection angle (in this case 242 mrad with the FEI HAADF detector), otherwise data will not be collected to the fullest extent. Probe array resolution also has a high impact on calculation duration.

The crystal slicing is adjusted by setting sub-slabs and slices per sub-slab. The slices determine which atoms are taken into consideration per scattering event during the multislice calculation. Ideally this value would be set to the number of atom layers within the crystal, but this might be a problem on

low memory computers. Increasing the number of sub-slabs lowers memory requirements, while increasing computation duration due to constant loading and saving of sub-slab potentials. The "center slices" checkbox can be activated if atoms are set directly at the crystal border. Depending on the model contrast values added by these atoms might be lost if this option is neglected.

The microscope parameters are chosen in accordance with values used in real measurements [19]. Most lens aberrations, spherical aberration in particular, are considered to be corrected.

The number of TDS runs (Thermal Diffusive Scattering) determines how many times the simulation will be repeated with added random thermal atom displacement in each simulation run. Considering TDS is critical in creating realistic results, but since calculation duration scales linearly with the number of TDS runs it should not be set to high. An investigation of TDS run influence on output data is done in section 4.1.

The detector collection angles are chosen to resemble those of detectors used in real measurements. The ranges have been determined by D. Knez [20] and are taken from his PhD thesis:

- **FEI HAADF:** $\theta_{inner} = 48$ mrad, $\theta_{outer} = 242$ mrad
- **Gatan HAADF:** $\theta_{inner} = 18$ mrad, $\theta_{outer} = 67$ mrad
- **Gatan ABF:** $\theta_{inner} = 9.5$ mrad, $\theta_{outer} = 22$ mrad

4.1 Investigating TDS Run Influence

Increasing the simulated TDS runs has a notable effect on detector intensities. A beryl sample with an Fe impurity and a thickness of $z = 11$ unit cells (i.e. about 10 nm) was simulated with 5, 10, 15 and 20 TDS runs in order to compare output intensities. These results were used to decide on a reasonable number of TDS runs to balance between calculation time and output quality.

The results were analyzed by integrating over the Fe intensities with the software Seek & Integrate [21]. The comparison of integration results for five and twenty TDS runs are shown in figures 8, 9 and 10.

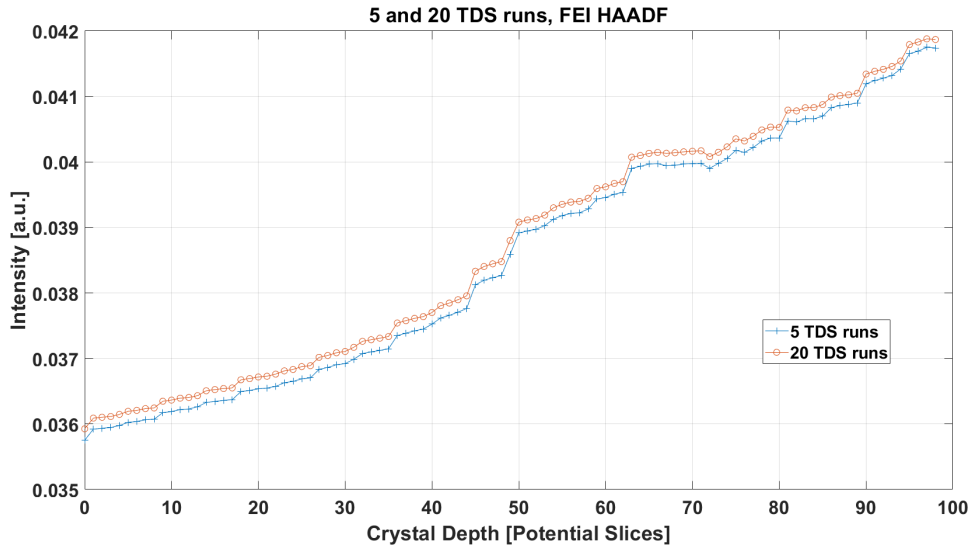


Figure 8: Comparison of intensities as a function of crystal thickness for the FEI HAADF detector. The y-axis shows the integrated intensity of the Fe atom. One atom slice is equal to 1.022 \AA .

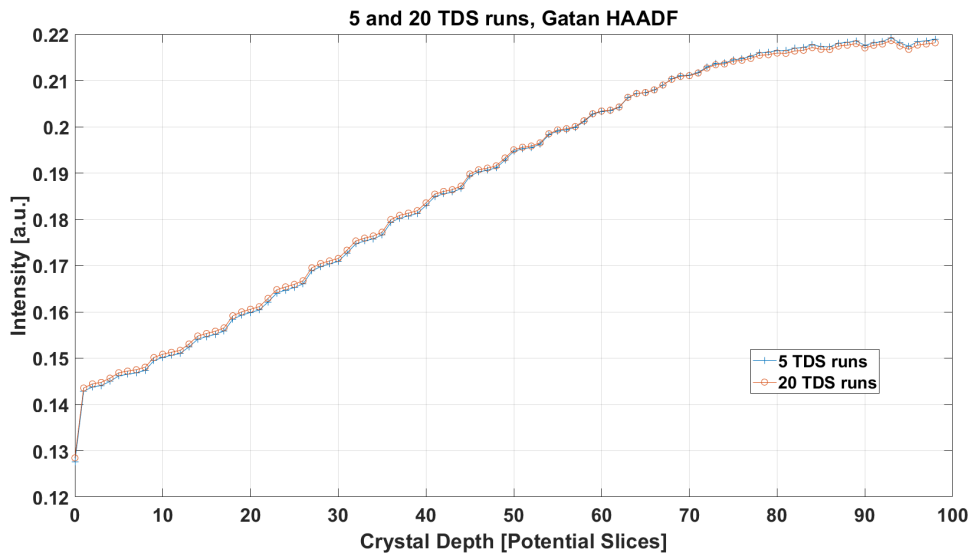


Figure 9: Comparison of intensities as a function of crystal thickness for the Gatan HAADF detector. The y-axis shows the integrated intensity of the Fe atom. One atom slice is equal to 1.022 \AA .

As seen in figure 8 the intensities for five and twenty TDS runs are qualitatively the same for the FEI HAADF detector, while the Gatan detector shows barely any difference at all. The Gatan ABF detector in figure 10 shows a greater difference for lower thicknesses, notice however that these differences occur in the second decimal place and therefore do not bear much weight.

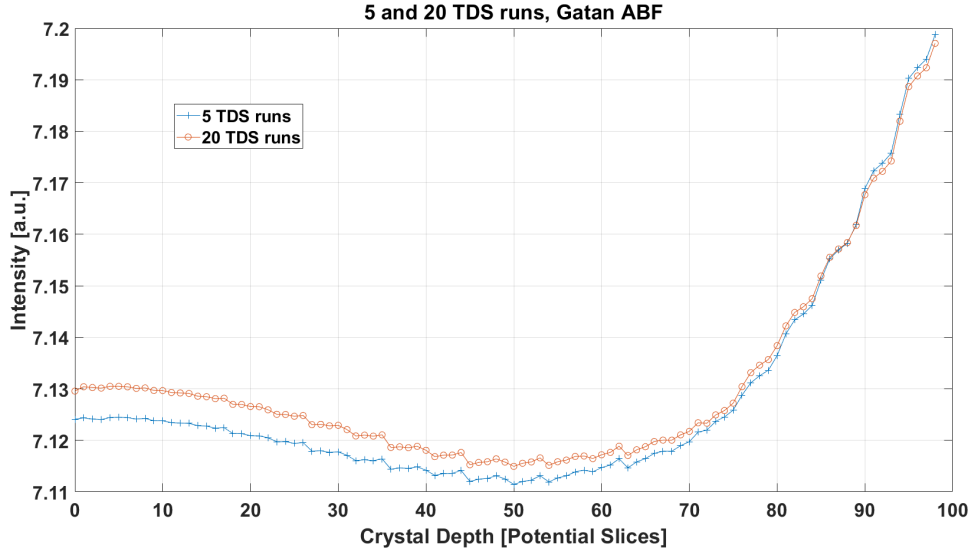


Figure 10: Comparison of intensities as a function of crystal thickness for the Gatan ABF detector. The y-axis shows the integrated intensity of the Fe atom. One atom slice is equal to 1.022 \AA .

Taking these results into consideration one can safely say that five TDS runs are enough for a realistic representation of intensity values, while also minimizing required calculation times.

5 Simulation Results

The results shown are projected images of the crystal at various thickness values with different dopant materials. The dopant materials analyzed are Cs, K, Li, as well as one, three and five Na atoms. Further simulations were done with the center channel filled with two Na per unit cell (66 Na in total) and one Na and one O atom per unit cell (33 Na & 33 O in total) respectively.

The simulations are performed on these atoms because they are most commonly detected in beryl samples. Although Fe and H_2O appear in beryl as well, simulations were not performed for these samples because H_2O simulation results were already obtained by C. Gspan and Fe only appears as substitute atom within the beryl crystal grid.

The crystal models used contain one of each dopant atom, unless stated otherwise. The atom placement is on the topside of the crystal within the first atomic layer in the channel at the center. Potential slice placement needs to be carefully adjusted in such a way, that the topmost layer potential is also taken into account to its full extent.

5.1 One Cs-Dopant

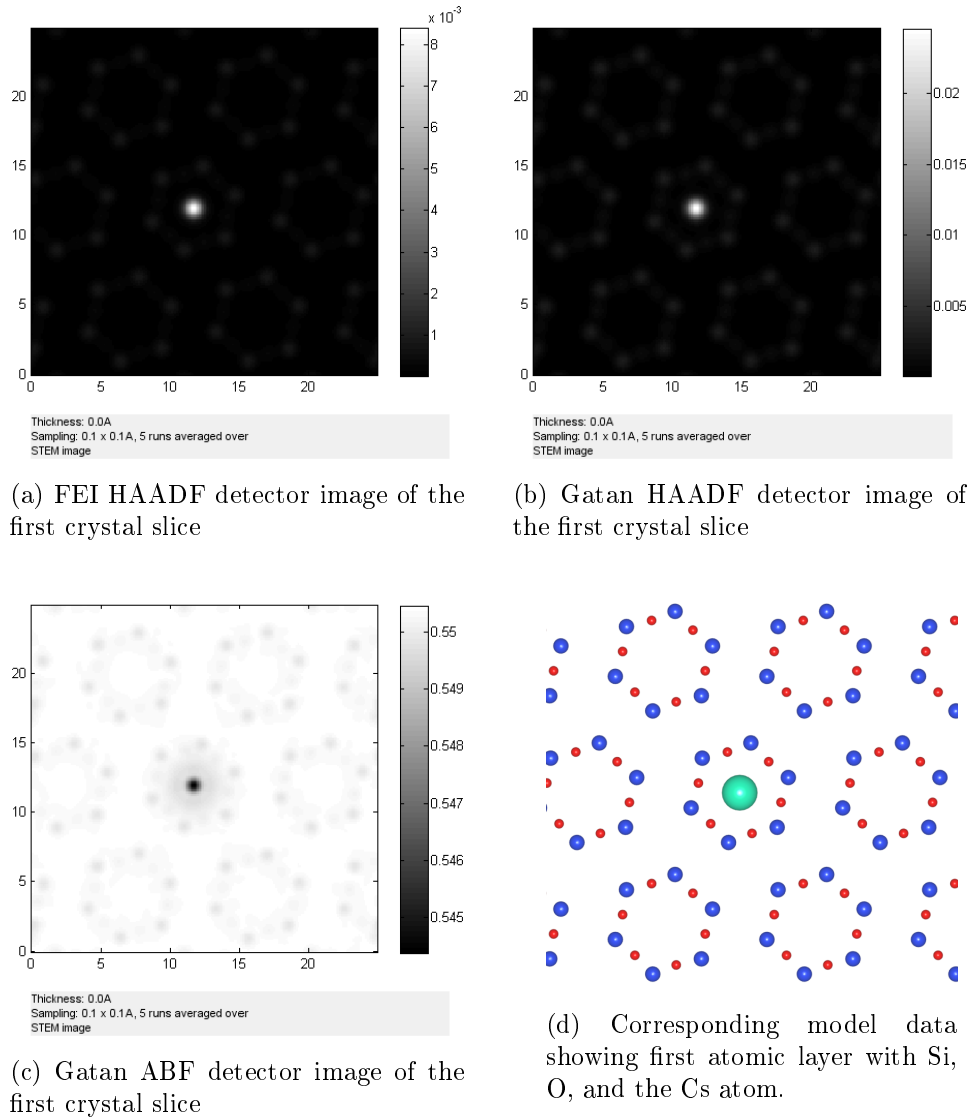


Figure 11: Simulated images for a beryl crystal with one dopant Cs atom showing the first atomic layer projection. The Corresponding model is shown for illustration purposes.

As seen in figure 11 the atomic positioning as well as the intensities fit the model data. As expected, the HAADF images show high contrast at the Cs position, while the ABF image shows low contrast values in the same position due to high angle scattering of the comparably heavy Cs atom.

The results become increasingly realistic compared to real STEM images with increasing simulated thickness. Real STEM images depict crystals with a thickness of approximately 20 to 30 nm. In order to illustrate the progression of image quality results are shown for increasing sample thickness for the Cs atom dopant.

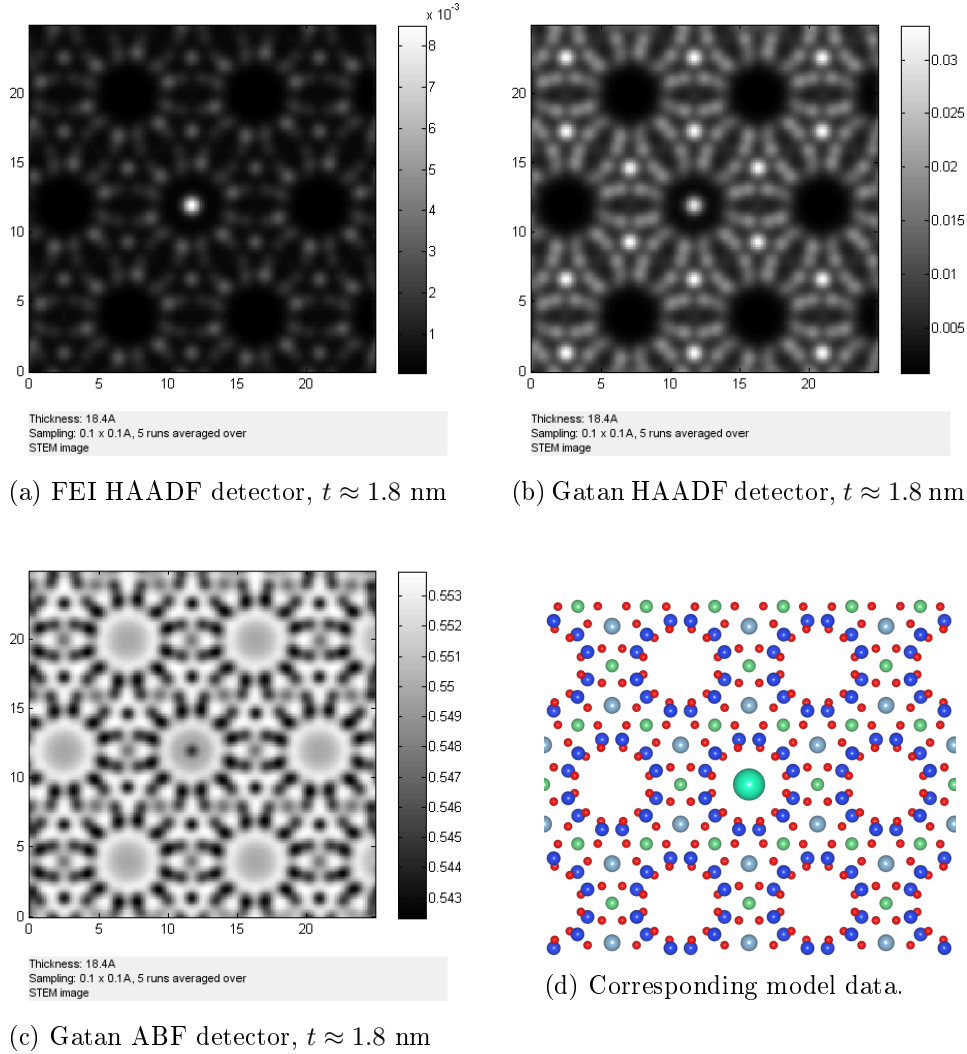


Figure 12: Simulated images for a beryl crystal with one dopant Cs atom showing the first two unit cells in projection. The Corresponding model is shown for illustration purposes.

Figure 12 shows the projection of the first two unit cells of the sample. With all atoms shown, one can clearly see that the Al intensities are the most dominant (next to Cs), which is to be expected since it has the highest Z value in the undoped beryl crystal. The Al intensities will increase compared to the Cs intensity, since the contrast for Al increases with increasing thickness, while the Cs contrast stems only from the single atom at the first atomic layer.

Even for such a thin sample the Gatan ABF detector shows high intensity for Be, which is not detected by the HAADF detectors.

Since the crystal model is shown in the c -direction and the simulated electron beam also propagates through the crystal in the c -direction, the model data and projected potential will appear to remain the same, while their only difference will be their thickness values.

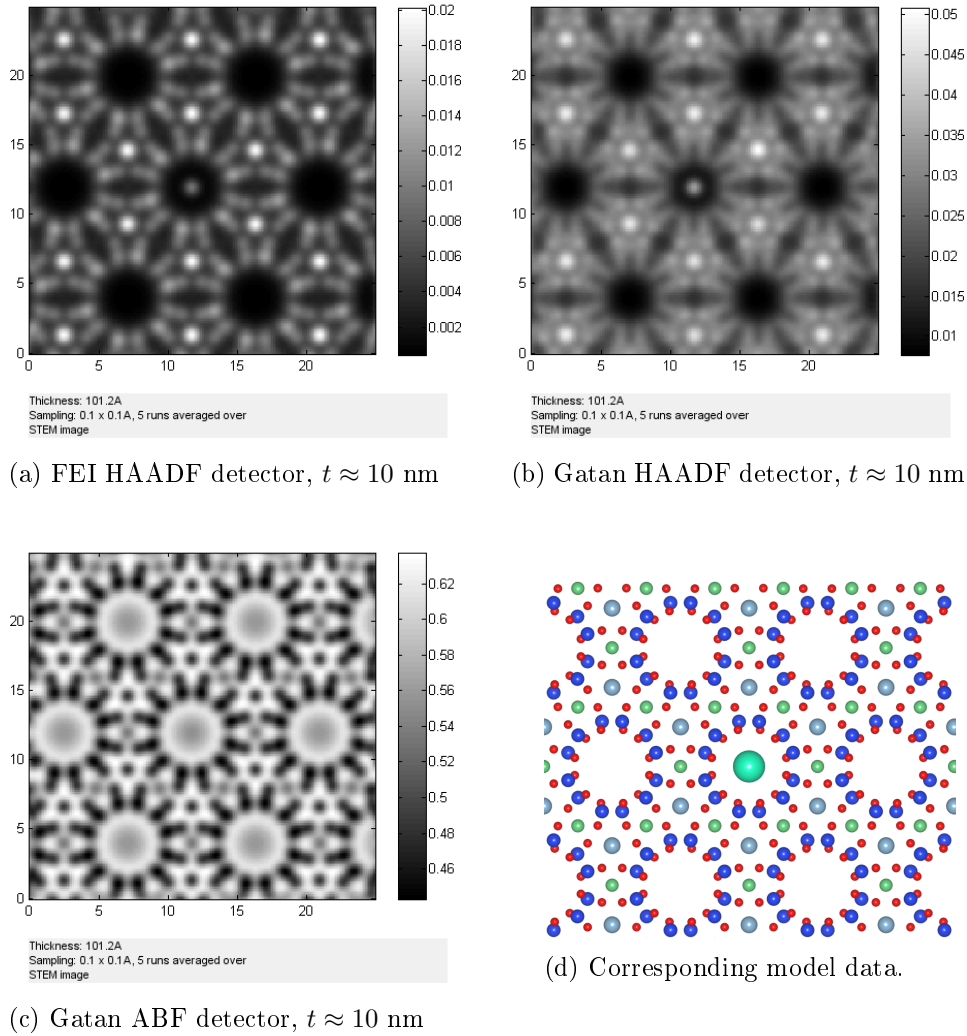


Figure 13: Simulated images for a beryl crystal with one dopant Cs atom showing the first eleven unit cells in projection. The Corresponding model is shown for illustration purposes.

The contrast values in figure 13 have changed significantly for each detector. The crystal now has a thickness of $t \approx 10$ nm. The FEI detector data show the Cs-atom relatively dark compared to the ever increasing Al intensities.

The Gatan HAADF contrast appears a bit smeared due to the auto-contrast feature of QSTEM and the similar intensities of the Al- and Cs atoms. This effect disappears with increasing thickness due to increasing Al-intensity.

The Gatan ABF image shows no visible trace of the Cs atom anymore. This might be due to the strong phase dependency of ABF images and the positioning of the Cs atom on the top of the crystal.

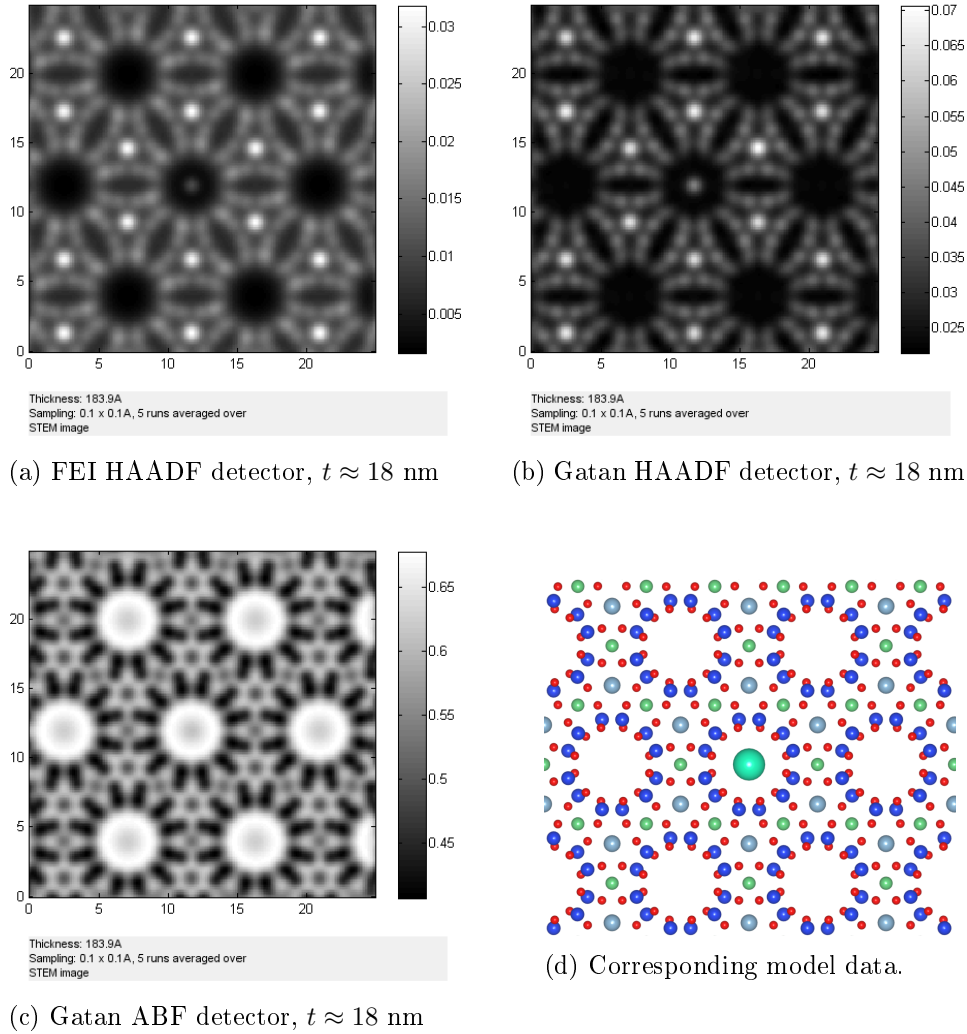


Figure 14: Simulated images for a beryl crystal with one dopant Cs atom showing the first 20 unit cells in projection. The Corresponding model is shown for illustration purposes.

Figure 14 shows lower intensity for the Cs atom position in the FEI HAADF detector than in the Gatan HAADF detector. This stems from the fact that the ratio of Cs intensity to Al intensity is lower in the FEI HAADF image than in the Gatan HAADF image. The difference in absolute intensity can only be shown by integrating over the images respectively, since the auto-contrast feature of QSTEM distorts the intensity values perceived by the naked eye.

The ABF contrast for lighter elements becomes more visible with increasing thickness, it is therefore possible to see the atom columns exhibiting the Be atoms. This is to be expected, since this detector is more susceptible for lighter elements like Be, Si and O. This fact is further highlighted by comparison of Al visibility in each of the three detectors.

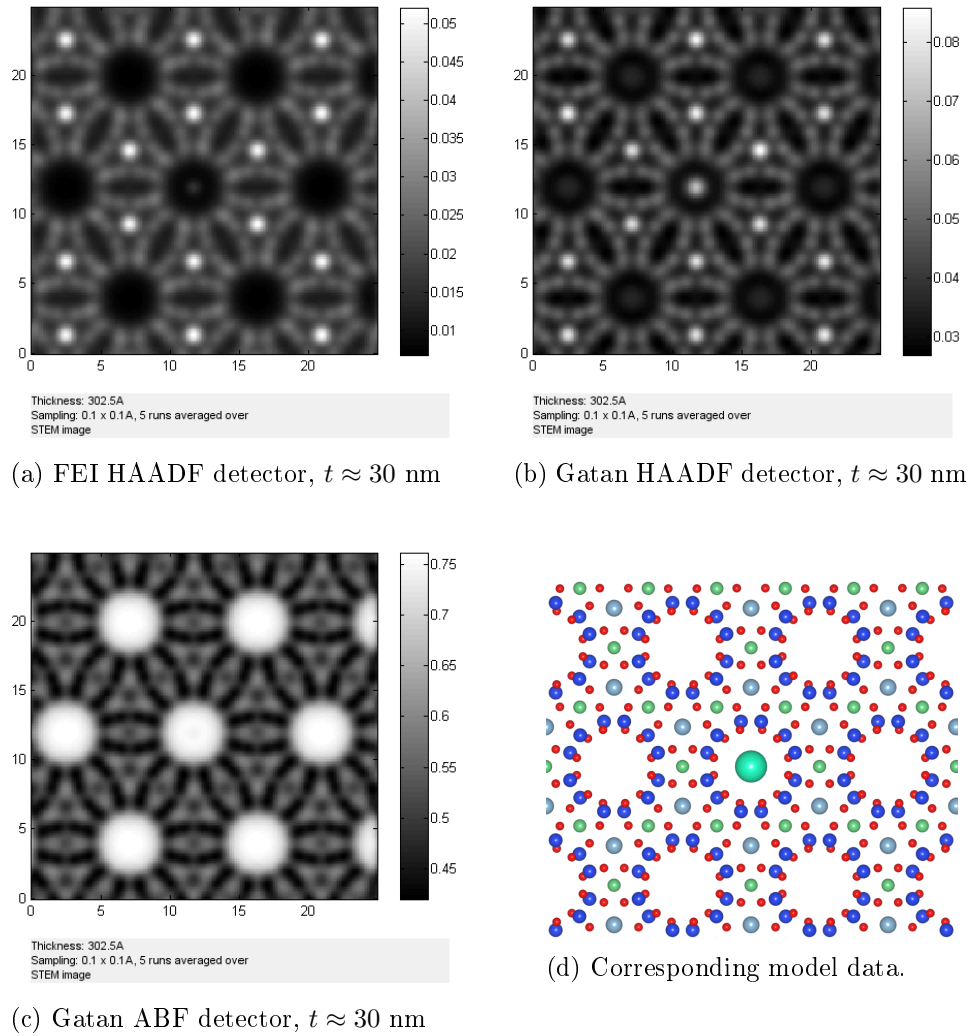
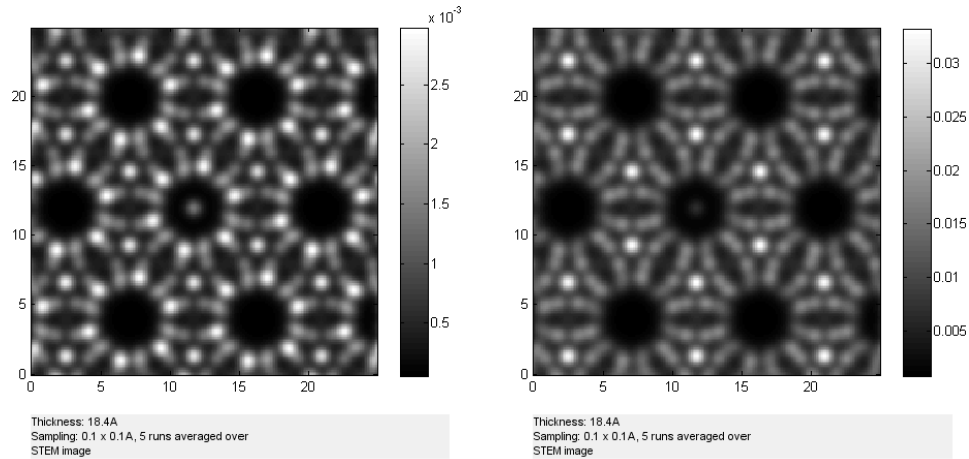


Figure 15: Simulated images for a beryl crystal with one dopant Cs atom showing all 33 unit cells in projection. The Corresponding model is shown for illustration purposes.

The FEI HAADF Cs intensity in figure 15 is barely visible anymore, while the Cs intensity for the Gatan HAADF detector appears to have increased with an increase of t from 18 nm to 30 nm. Notice however, that the empty channels in the Gatan HAADF image begin to show moderate contrast values as well. This channel contrast superimposed with the Cs contrast might be the reason for the increased intensity shown. The evaluation of the images in section 6 will also cover a comparison of dopant to channel intensity as further investigation.

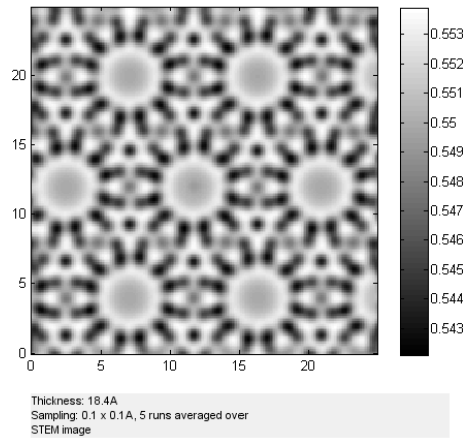
While the Gatan HAADF detector begins to show unexpected behaviour, the Gatan ABF detector results behave as expected. Contrast values in the empty channels increase, while the lighter elements become more dominant and cut clear contours into the image.

5.2 One K-Dopant

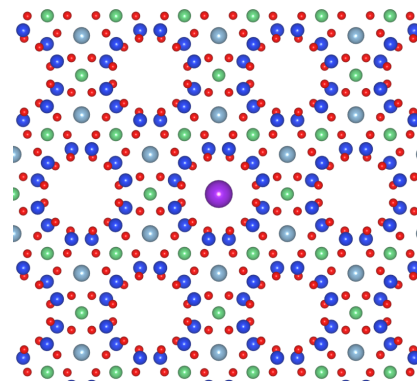


(a) FEI HAADF detector image of the first two unit cells, $t \approx 1.8$ nm

(b) Gatan HAADF detector image of the first two unit cells, $t \approx 1.8$ nm



(c) Gatan ABF detector image of the first two unit cells, $t \approx 1.8$ nm



(d) Corresponding model data.

Figure 16: Simulated images for a beryl crystal with one dopant K atom showing the first two unit cells in projection. The Corresponding model is shown for illustration purposes.

Figure 16 clearly shows that the dopant intensity is already very low compared to the Cs intensity from figure 12. Even with low crystal thickness the Al- and Si intensities begin to overshadow the dopant contrast. The Gatan HAADF image already shows little trace of the K atom, similarly to the Gatan ABF image, where the K atom is apparent only upon close inspection.

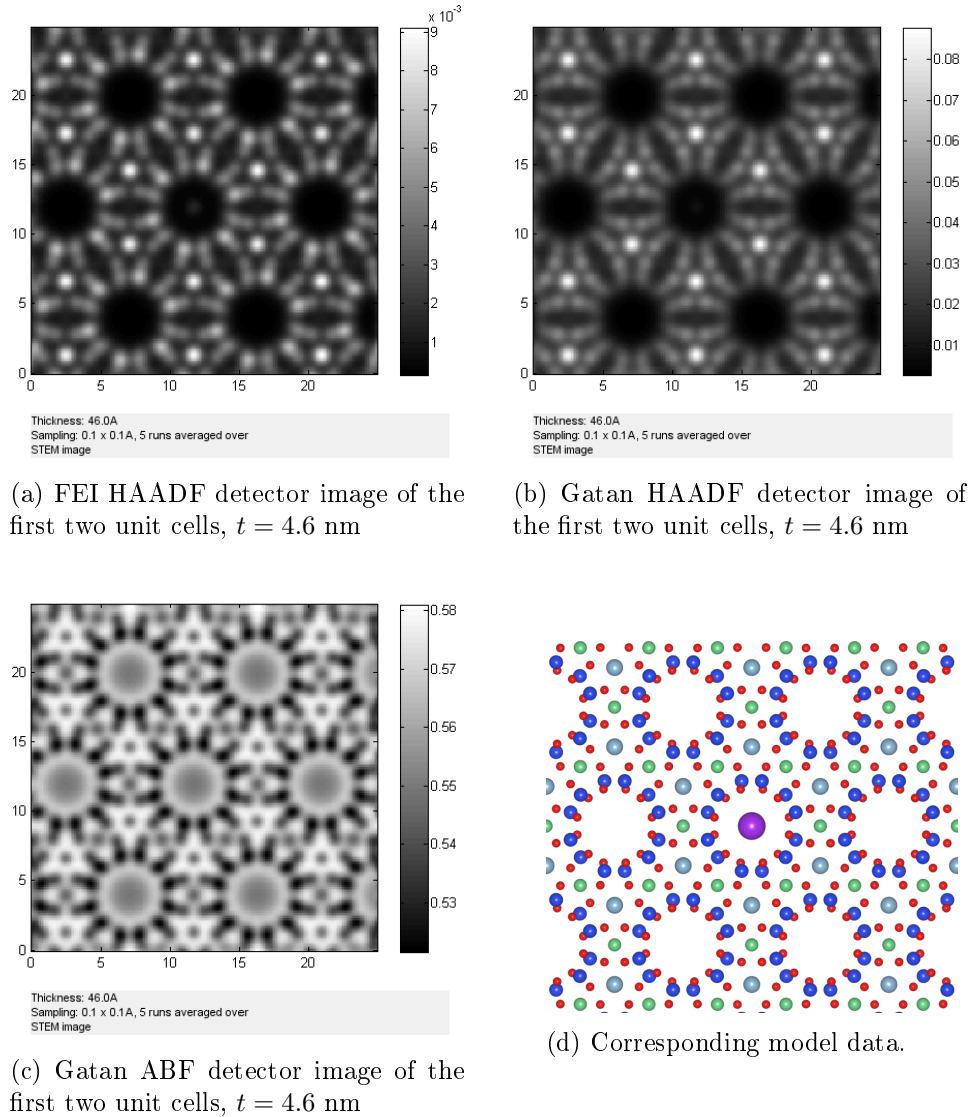


Figure 17: Simulated images for a beryl crystal with one dopant K atom showing the first five unit cells in projection. The Corresponding model is shown for illustration purposes.

As seen in figure 17, the K atom is already basically invisible at thicknesses of $t = 4.6$ nm. While the FEI HAADF detector still shows a trace of the dopant atom, the Gatan HAADF and ABF detectors show no visible trace of K anymore.

Lower visibility is expected for lower atomic numbers, which leads to the fact that lower Z atoms are only detectable for very thin samples or for stacks of dopant atoms inside the channels.

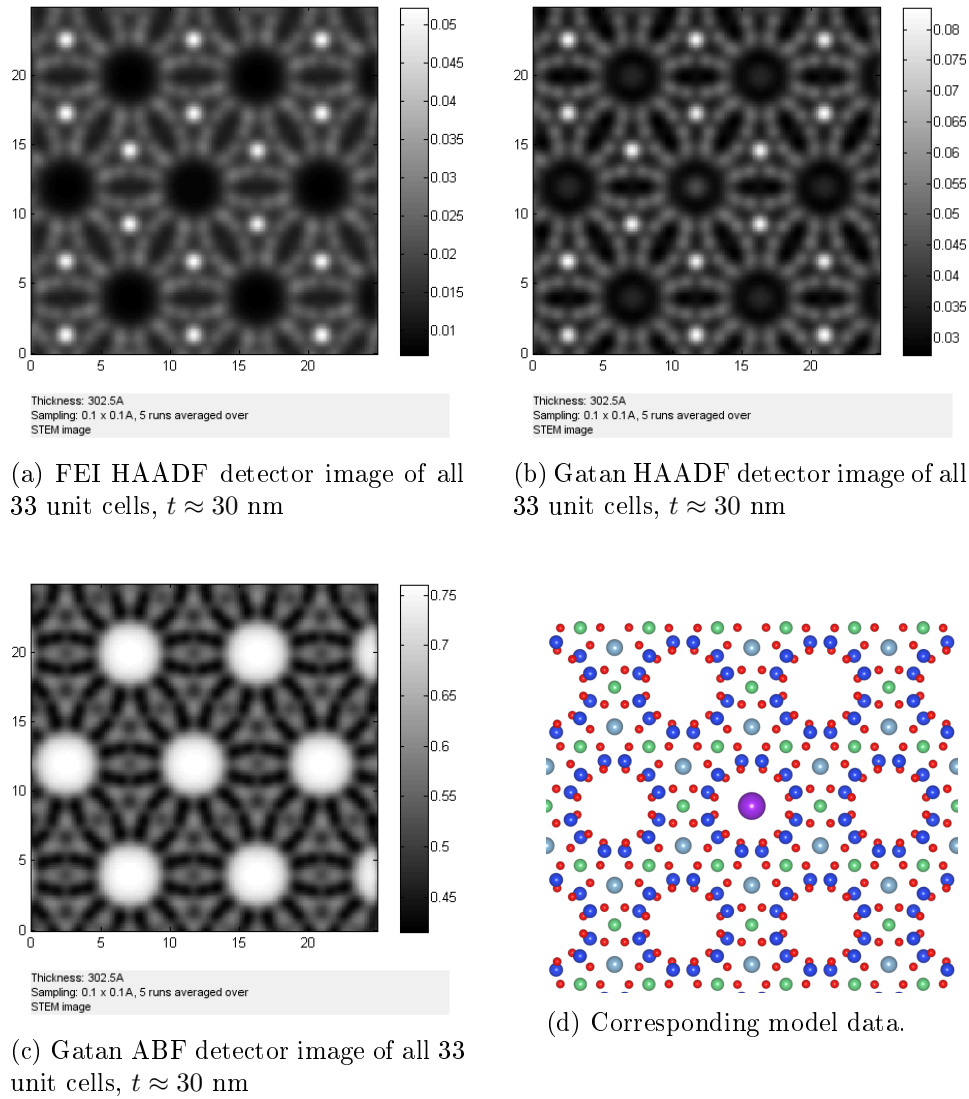
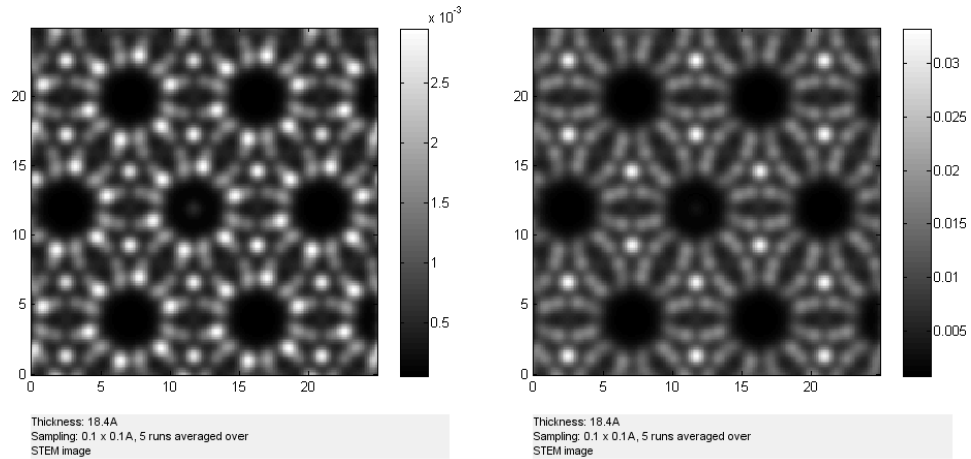


Figure 18: Simulated images for a beryl crystal with one dopant K atom showing all 33 unit cells in projection. The Corresponding model is shown for illustration purposes.

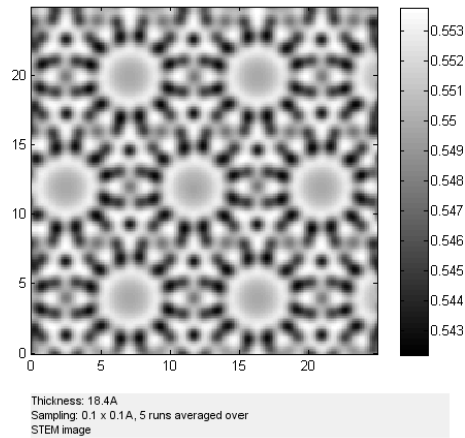
While the contrast visibility in the FEI HAADF and Gatan ABF detectors for the dopant atom is completely gone for $t \approx 30$ nm, figure 18b clearly shows channel contrast for the Gatan HAADF detector, similar to the Gatan HAADF image for Cs in figure 15b. The channel filled with a single K atom is also easily discernable with the naked eye, while the other detectors show no trace of K.

5.3 One Na-Dopant

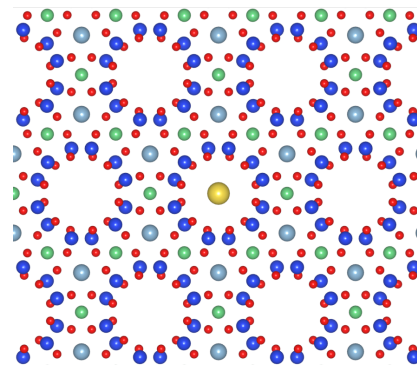


(a) FEI HAADF detector image of two unit cells, $t \approx 1.8$ nm

(b) Gatan HAADF detector image of two unit cells, $t \approx 1.8$ nm



(c) Gatan ABF detector image of two unit cells, $t \approx 1.8$ nm



(d) Corresponding model data.

Figure 19: Simulated images for a beryl crystal with one dopant Na atom showing the first two unit cells in projection. The Corresponding model is shown for illustration purposes.

As seen in figure 19 the dopant is basically invisible even at very low thicknesses. Only the FEI HAADF detector hints at the presence of Na inside the channel.

Based on this it is safe to say that one should not expect to see single Na atoms in detector images of realistically sized beryl samples.

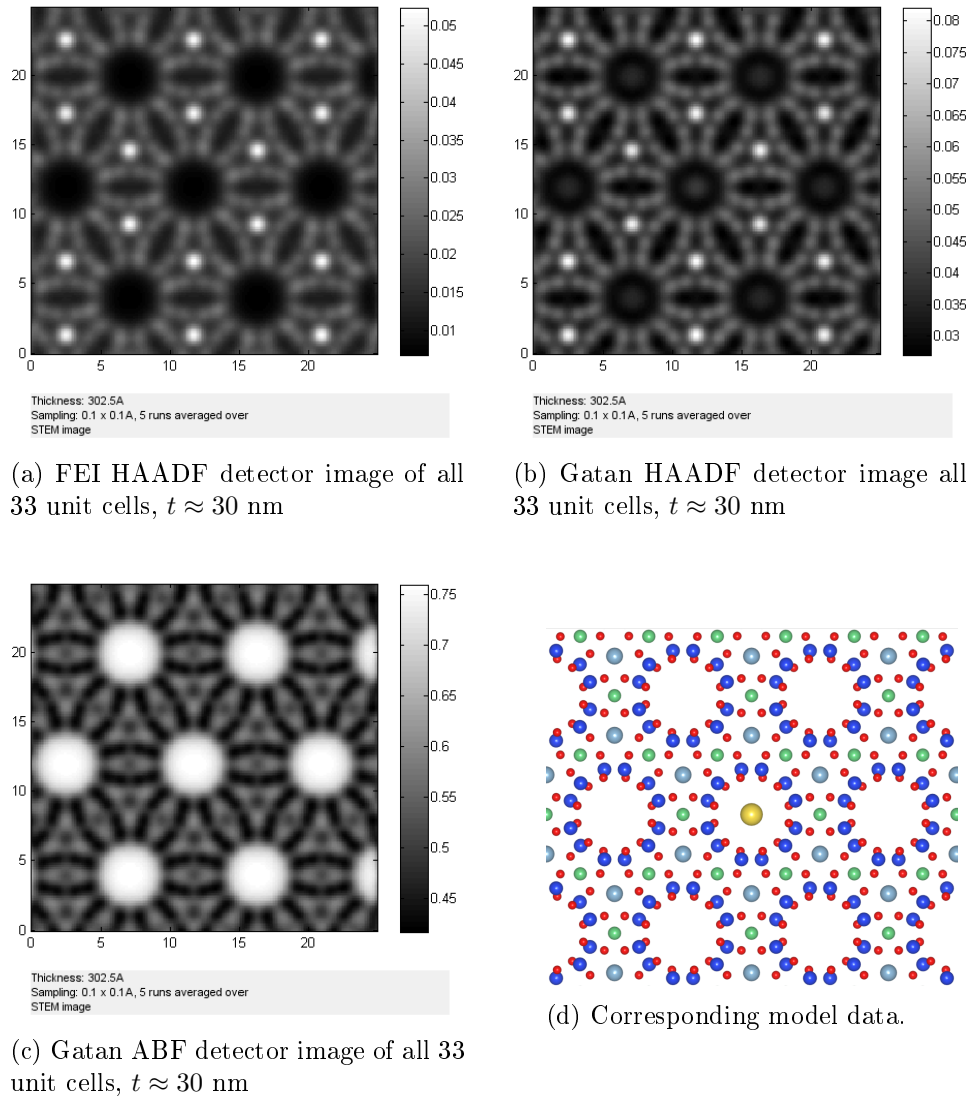


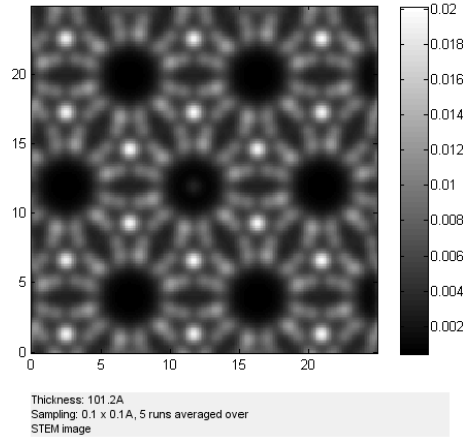
Figure 20: Simulated images for a beryl crystal with one dopant Na atom showing all 33 unit cells in projection. The Corresponding model is shown for illustration purposes.

With the Na contrast gone with very low thicknesses one can also not see any hints of Na with $t \approx 30$ nm. This result does illustrate the channel contrast in the Gatan HAADF detector as seen in figure 20b, however.

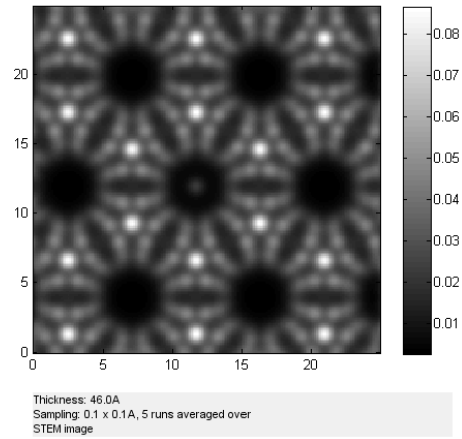
Even with channel contrast it is basically impossible to discern between filled and empty channels.

5.4 Five Na-Dopants

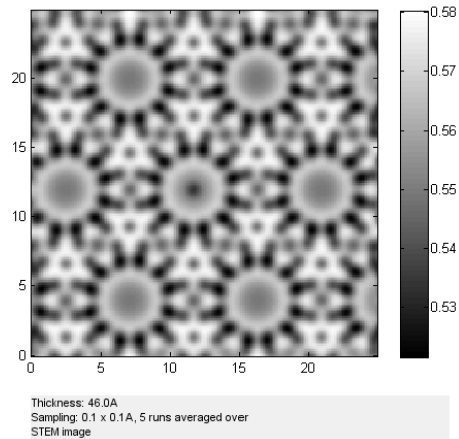
The following sample contains five Na atoms, stacked on top of each of the first five unit cells.



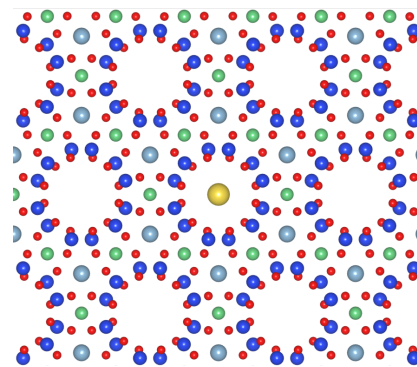
(a) FEI HAADF detector image of eleven unit cells, $t \approx 10$ nm



(b) Gatan HAADF detector image of eleven unit cells, $t \approx 10$ nm



(c) Gatan ABF detector image of eleven unit cells, $t \approx 10$ nm



(d) Corresponding model data.

Figure 21: Simulated images for a beryl crystal with five dopant Na atoms showing the first eleven unit cells in projection. One Na atom is placed at the top of each of the first five unit cells. The Corresponding model is shown for illustration purposes.

As expected, figure 21 shows increased intensities for the dopant atom with five Na atoms stacked instead of one. The contrast cutoff for the dopant contrast for the FEI HAADF detector happens further down in the material as well, namely at $t \approx 10$ nm instead of $t \approx 1.8$ nm.

Another notable result is the fact that the Gatan HAADF contrast never vanishes across the whole thickness range of 33 unit cells, as opposed to the one Na and one K samples, for instance.

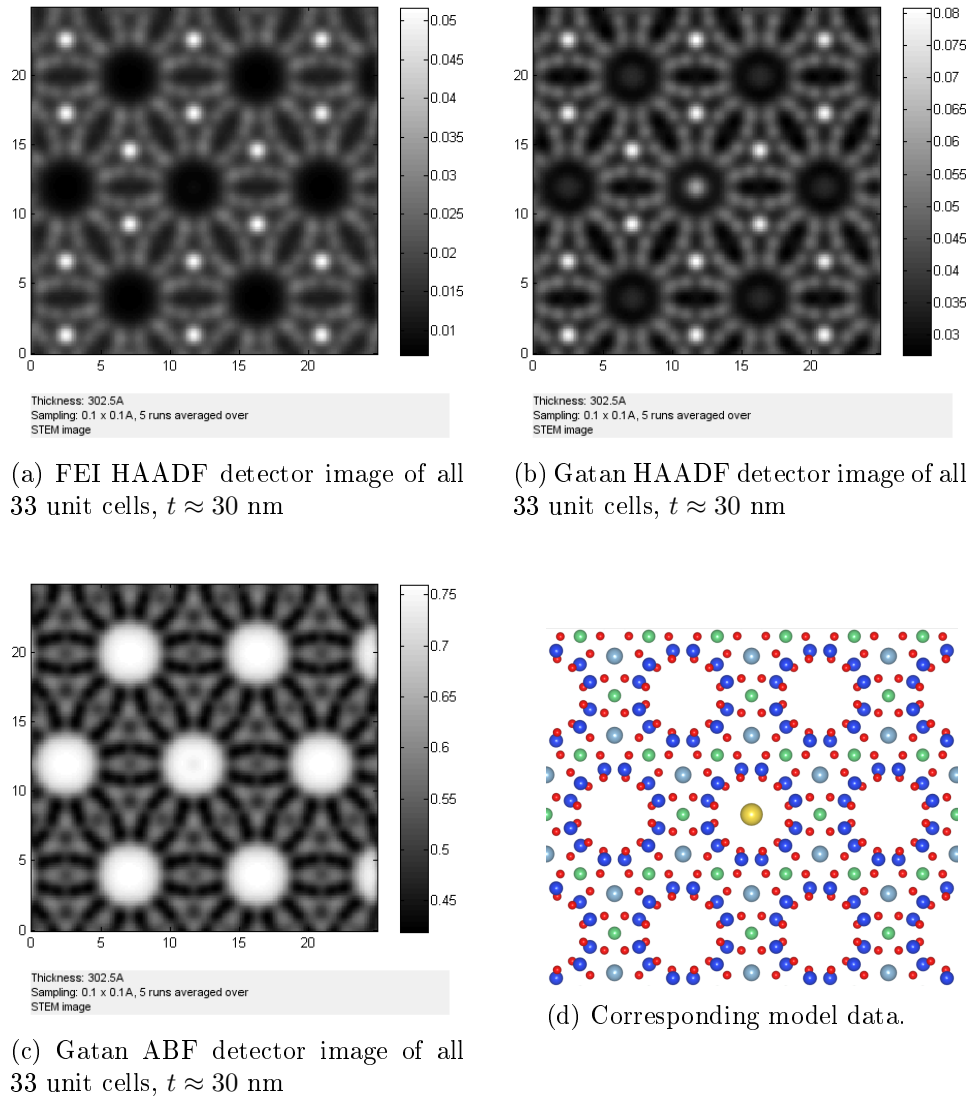
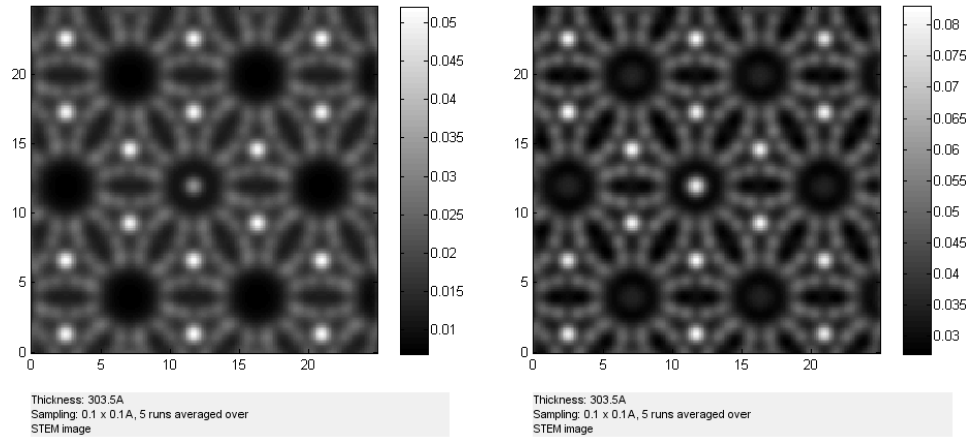


Figure 22: Simulated images for a beryl crystal with five dopant Na atoms showing all 33 unit cells in projection. One Na atom is placed at the top of each of the first five unit cells. The Corresponding model is shown for illustration purposes.

With increasing thickness the channel contrast in the Gatan HAADF image is rising again. This time, due to the increase in number of dopant atoms, channel contrast allows the differentiation of dopant to channel contrast, unlike for the crystal with only one Na atom.

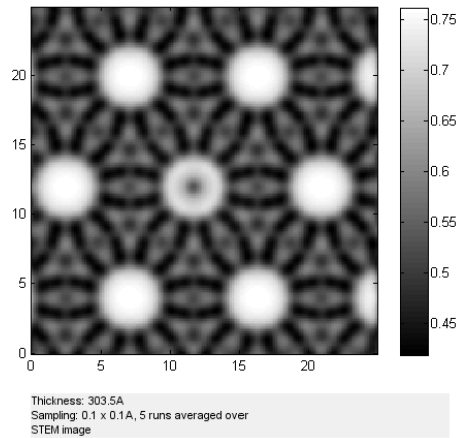
Also note that the increase in dopant contrast is not due to QSTEMs auto-contrast feature but due to real intensity increase. The contrast scaling is set by the Al intensity, which remains the same throughout simulations. This implies that the dopant contrast rises with increasing thickness due to channel contrast. This will be further evaluated numerically in section 6.

5.5 66 Na-Dopants

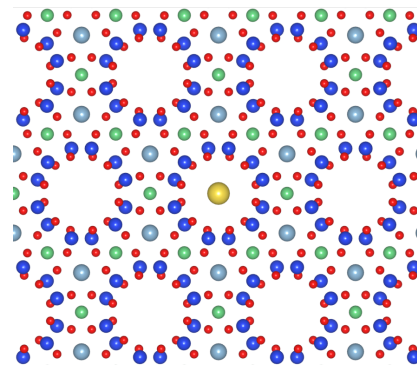


(a) FEI HAADF detector image of all 33 unit cells, $t \approx 30$ nm

(b) Gatan HAADF detector image of all 33 unit cells, $t \approx 30$ nm



(c) Gatan ABF detector image of all 33 unit cells, $t \approx 30$ nm



(d) Corresponding model data.

Figure 23: Simulated images for a beryl crystal with 66 dopant Na atoms showing all 33 unit cells in projection. Two Na atoms are placed within each unit cell at the same height as the Al atoms. The Corresponding model is shown for illustration purposes.

Figure 23 shows the results for a channel filled with Na to its maximum capacity. Neither of the three detectors show an intensity cutoff for the Na intensity, since there are two Na atoms added per unit cell across the whole crystal. The contrast for the FEI HAADF detector appears to be relatively constant across the whole thickness range, which will be further illustrated in section 6.

It is clear to see that a fully filled channel is easy to detect with any of the three detectors, even with elements as light as Na. This is also the first simulated sample for which a clear intensity signal is visible for the Gatan ABF detector at a thickness of $t \approx 30$ nm.

6 Data Evaluation and Interpretation

The detector images shown in section 5 are not the only data available for evaluation. Any simulation performed yields an image for each detector and each atomic layer within the crystal, resulting in 297 images per detector for a crystal consisting of 33 unit cells stacked in c-direction.

Since the progression takes place in a well defined direction with a known distance covered per step ($\Delta t = 1.022 \text{ \AA}$) the evaluation of intensities for each atomic layer is a natural first step in analyzing the acquired data.

While the sheer amount of data gives invaluable insights into intensity progression, handling it without automatized methods is practically impossible. Therefore the software package Seek & Integrate [21] by D. Knez was used to automatically integrate over selected spots. The resulting integration values are stored within .xls files and automatically evaluated with MATLAB afterwards. The code for automatic evaluation of the .xls files is depicted in the appendix.

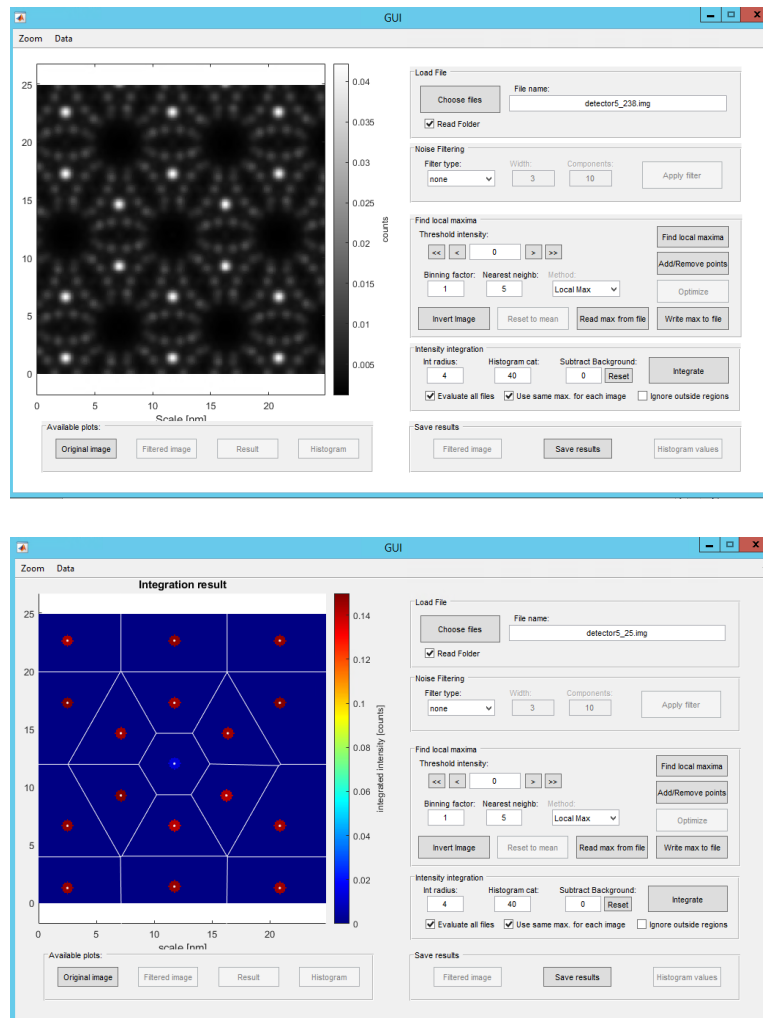
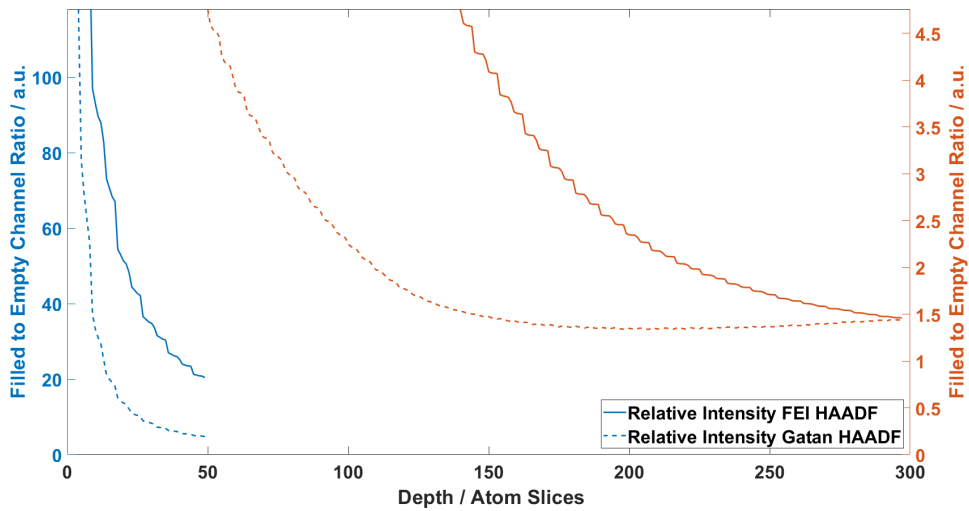


Figure 24: User interface of Seek & Integrate. Integration positions are chosen via the GUI or by writing them manually in a .csv file. This example integrates over Al and dopant atoms.

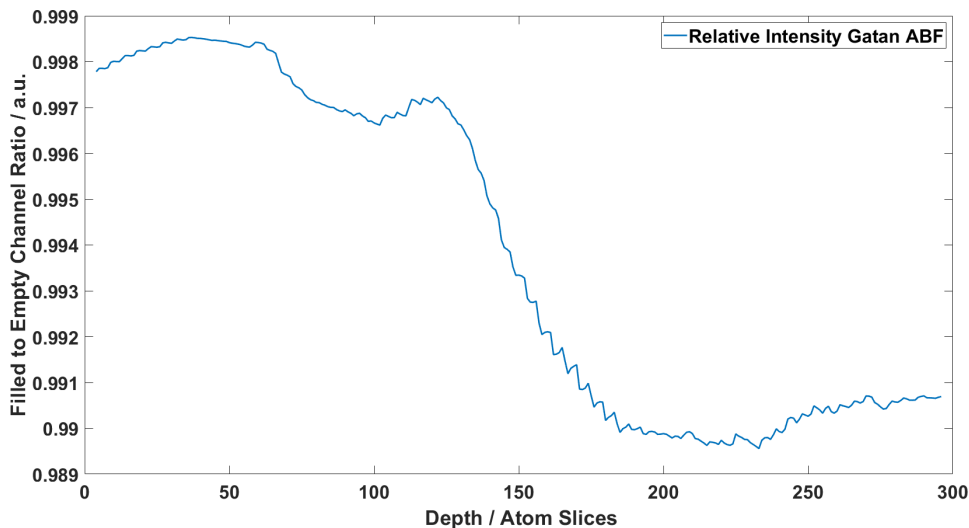
Performing the evaluation consists of integrating over the dopant atom, the Al columns and the empty channels shown in each detector image. The ratio of the dopant atom intensity and the Al intensity/channel intensity is then plotted as a function of crystal potential slice, which is equivalent to one atomic layer for simulations done in this thesis.

6.1 One Cs-Dopant

The following plots show the results for the three detectors, either for the ratio of dopant to Al or dopant to channel intensity.

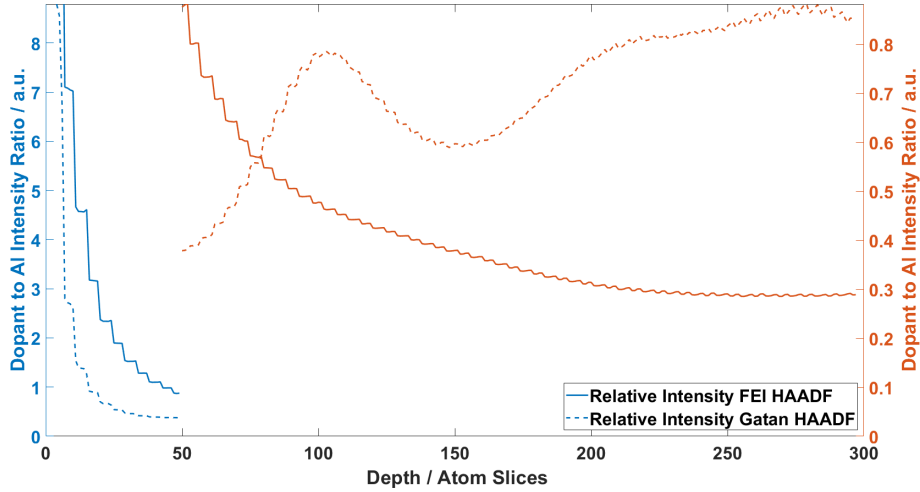


(a) FEI and Gatan HAADF intensity ratio of Cs to channel intensity. One atom slice is equal to 1.022 \AA .

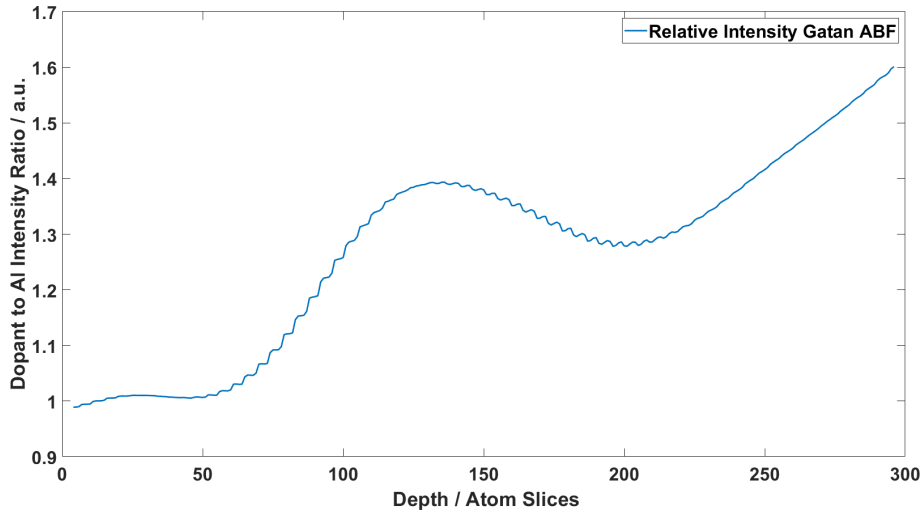


(b) Gatan ABF intensity ratio of Cs to channel intensity.

Figure 25: Ratio of integral results between Cs and channel intensity as a function of crystal slices. One atom slice is equal to 1.022 \AA .



(a) FEI and Gatan HAADF intensity ratio of Cs to Al intensity. One atom slice is equal to 1.022 Å.



(b) Gatan ABF intensity ratio of Cs to Al intensity.

Figure 26: Ratio of integral results between dopant and Al intensity as a function of crystal slices. One atom slice is equal to 1.022 Å.

As seen in figure 26 the Gatan HAADF detector behaves differently than the FEI HAADF detector starting at 5 nm thickness. This is an indication for the presence of channel contrast. As expected, the dopant intensity recedes for increasing thickness, but the background channel intensity increases the dopant intensity, leading to higher integral values than expected.

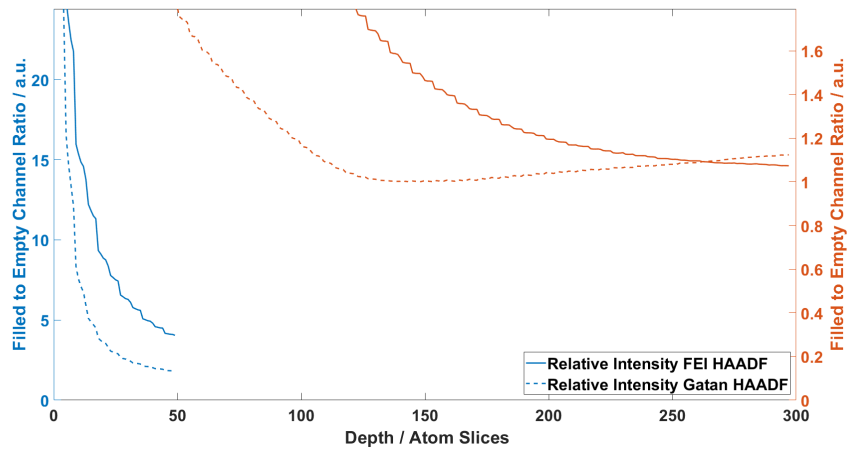
This hypothesis is further supported by the fact that the same increase is not seen in figure 25. With increasing dopant intensity the empty channel intensity rises as well, which cancels out the dopant intensity increase.

The behaviour of the Gatan HAADF detector is further explained by irregular thickness dependent variation of the Al signal starting at 5 nm. This variation is barely noticeable for the FEI HAADF detector, which is why only this detector can be used reliably for dopant intensity comparison to Al atoms.

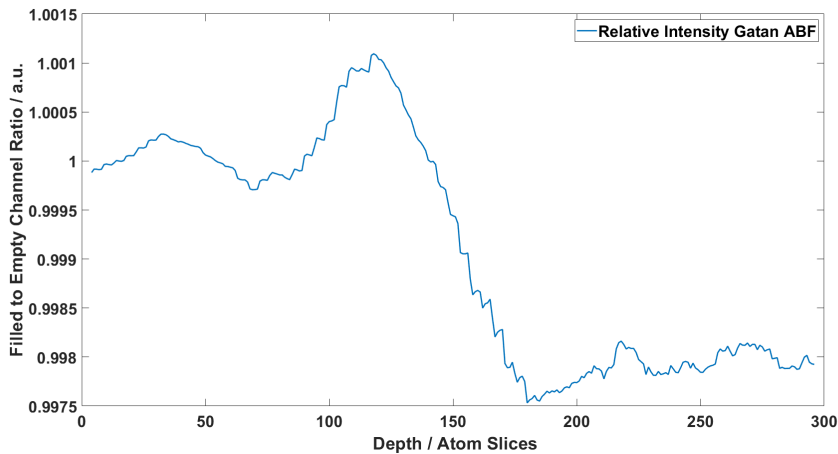
6.2 One K-Dopant

As seen in figure 27, the intensity ratio is qualitatively equal to the Cs sample in figure 25. The only difference is the maximum ratio of dopant to channel intensity, which is smaller by a factor of six for the K atom.

The intensity ratio for the FEI- and Gatan HAADF detectors are smoothly declining, while the Gatan ABF intensity shows irregular behaviour. This is due to the nature of the detector, which shows high intensity for weak scatterers in the low angle regime, which leads to empty channels appearing bright.



(a) FEI and Gatan HAADF intensity ratio of K to channel intensity. One atom slice is equal to 1.022 Å.

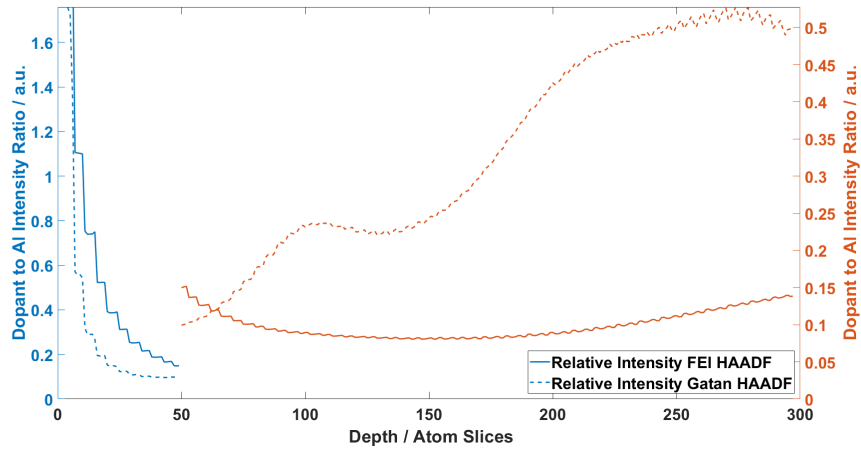


(b) Gatan ABF intensity ratio of K to channel intensity.

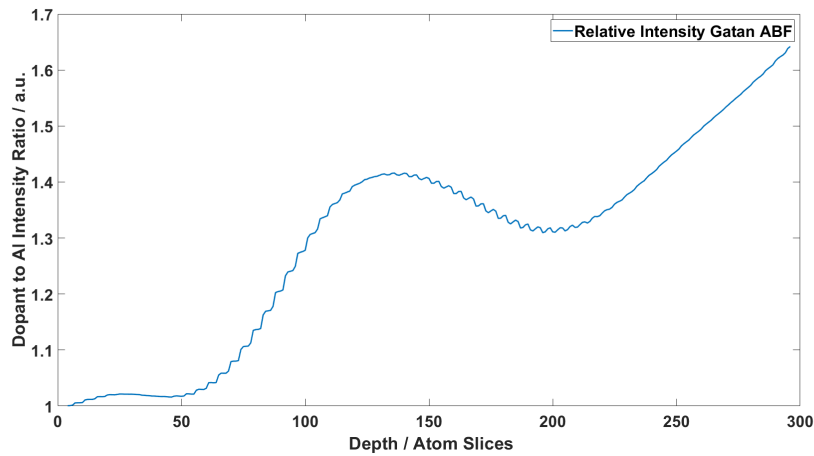
Figure 27: Ratio of integral results between dopant and channel intensity as a function of crystal slices. One atom slice is equal to 1.022 Å.

Integration over this area would therefore compare the brighter channel intensity to the darker dopant intensity, but with ratios very close to one, since the channel intensity dominates in the integral of filled *and* empty channels.

This is clearly seen in figure 27, where the ratio of dopant to channel is very close to one due to the weak intensity signal from the K atom.



(a) FEI and Gatan HAADF intensity ratio of K to Al intensity. One atom slice is equal to 1.022 Å.



(b) Gatan ABF intensity ratio of K to Al intensity.

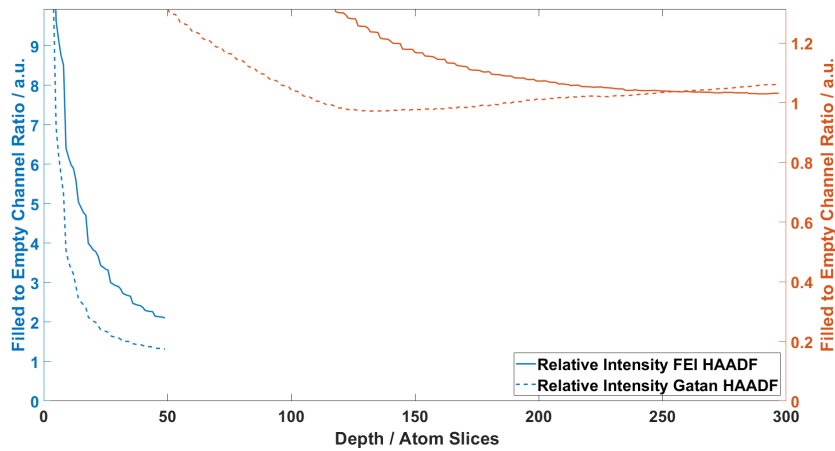
Figure 28: Ratio of integral results between dopant and Al intensity as a function of crystal slices. One atom slice is equal to 1.022 Å.

As seen in figure 28, the K atom sample exhibits the same channel intensity as the Cs sample, but with even better visibility. This is the case maximum intensity ratio of K to Al is lower, which leads to better y-axis scaling for higher crystal thicknesses. Another reason is the lower K intensity compared to Cs, which gives the channel intensity a higher relative impact.

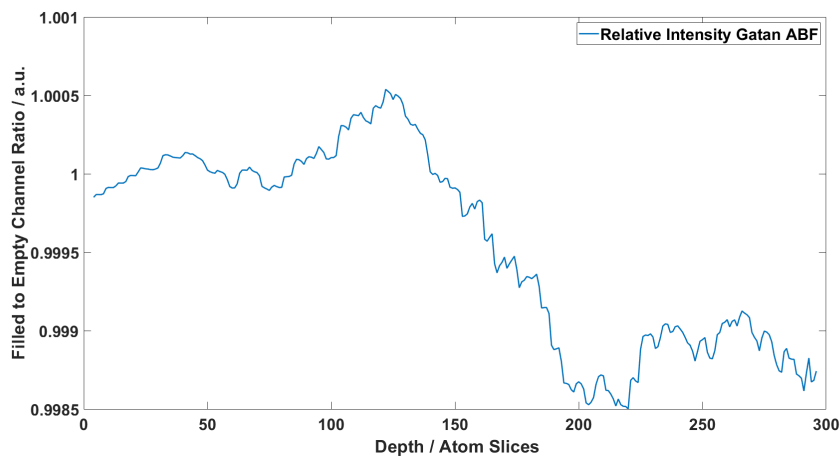
6.3 One Na-dopant

The most apparent difference between the samples Na and K from figure 29 is the magnitude of the intensity ratio, which is higher for the K sample. Other than that the qualitative decline for the FEI and Gatan HAADF detector is very similar for both samples.

Interestingly enough the Gatan ABF image is also very similar to the K sample. While the irregular behaviour of the intensity curve appears to be random in its progression, one should not be surprised by this result. The setup for both simulations is the same after all, except for the dopant being Na instead of K, which are both light elements.

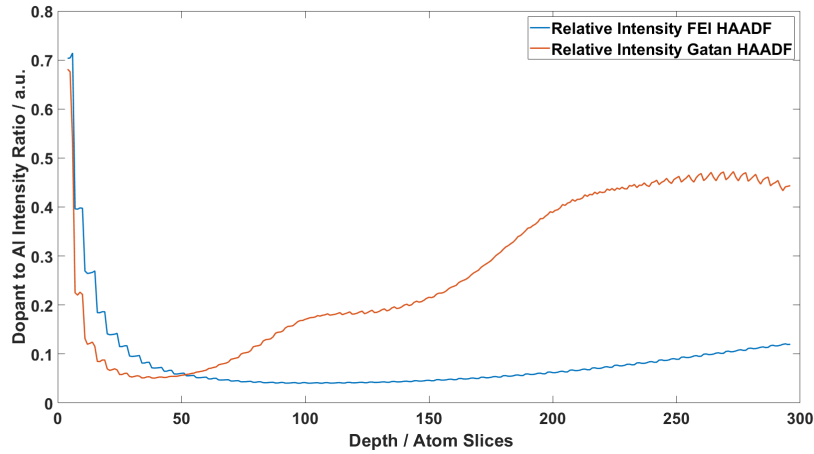


(a) FEI and Gatan HAADF intensity ratio of one Na to channel intensity. One atom slice is equal to 1.022 \AA .

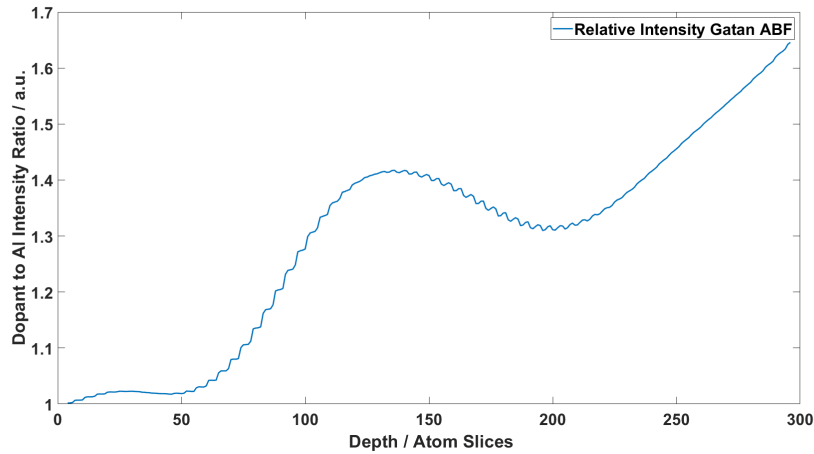


(b) Gatan ABF intensity ratio of one Na to channel intensity.

Figure 29: Ratio of integral results between dopant and channel intensity as a function of crystal slices. One atom slice is equal to 1.022 \AA .



(a) FEI and Gatan HAADF intensity ratio of one Na to Al intensity. One atom slice is equal to 1.022 \AA .



(b) Gatan ABF intensity ratio of one Na to Al intensity.

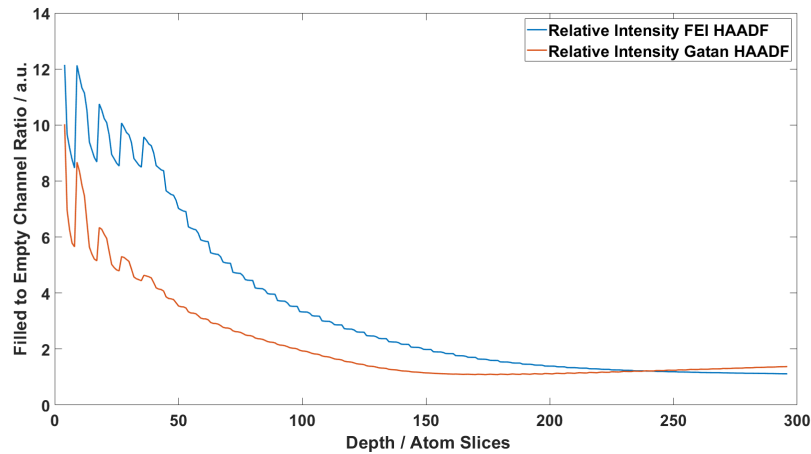
Figure 30: Ratio of integral results between dopant and Al intensity as a function of crystal slices. One atom slice is equal to 1.022 \AA .

The channel intensity for one Na atom is highlighted even more for the Gatan HAADF detector. This is again the case due to different y-axis scaling and lower intensity of the Na atom compared to K.

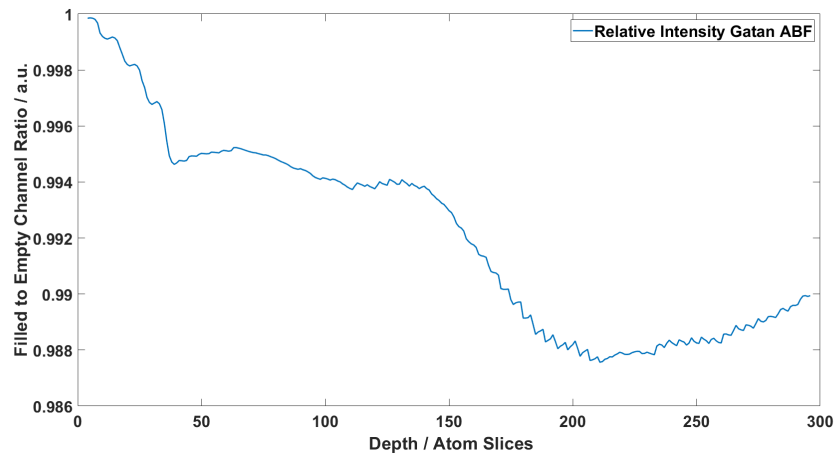
Notice that the ABF images for one Na and K are basically identical. The integrals of the dopants are very high, since one single Na or K atom have little impact on the ABF image for higher thicknesses. Since the comparison of two high integrals with the lower integrals of Al have a similar ratio, the resulting intensity curves are similar as well.

6.4 Five Na-Dopants

With the increased number of dopant atoms one can notice a qualitative change in the intensity ratio curves. For the FEI- and GATAN HAADF detectors the intensity cutoff has shifted to higher thicknesses, for instance. Also notable are the five peaks in the beginning of the intensity curves, which denote where the five dopant atoms are positioned within the sample. With the crystal thickness increasing, the number of dopant atoms at discrete sites increases as well. After five peaks there are no further dopants in the sample, at which point a regular decline of the intensity ratio sets in.



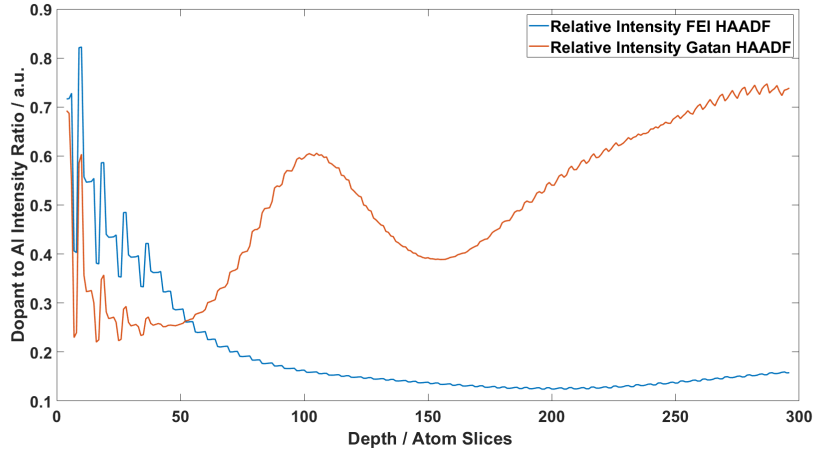
(a) FEI and Gatan HAADF intensity ratio of five Na to channel intensity. One atom slice is equal to 1.022 \AA .



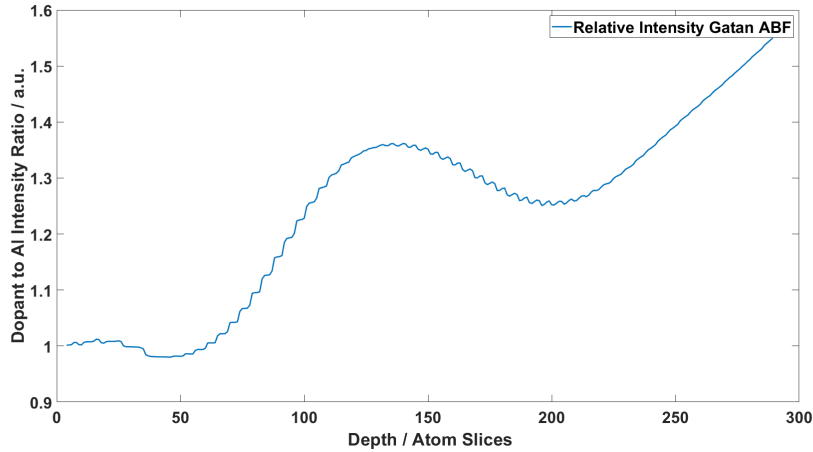
(b) Gatan ABF intensity ratio of five Na to channel intensity.

Figure 31: Ratio of integral results between dopant and channel intensity as a function of crystal slices. One atom slice is equal to 1.022 \AA .

The Gatan ABF image also shows a hint of the five dopant Na atoms, as the decline of the intensity ratio is steep below 50 slices, while it stabilizes again afterwards.



(a) FEI and Gatan HAADF intensity ratio of five Na to Al intensity. One atom slice is equal to 1.022 \AA .



(b) Gatan ABF intensity ratio of five Na to Al intensity.

Figure 32: Ratio of integral results between dopant and Al intensity as a function of crystal slices. One atom slice is equal to 1.022 \AA .

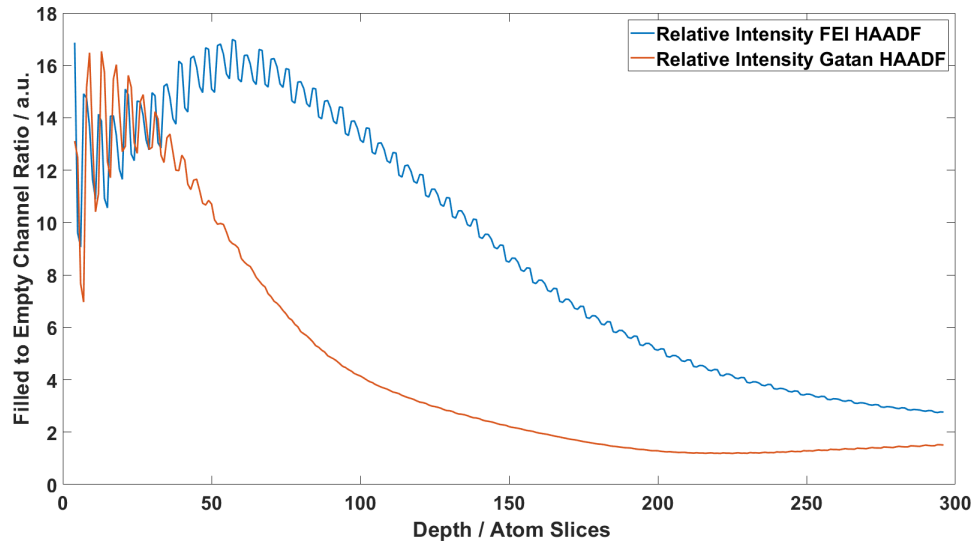
The dopant atom peaks are even more distinct when comparing the dopant intensity to the Al intensity, as the intensities are similar in magnitude, which leads to small differences having higher impacts on ratios.

While the intensity ratio of dopant to Al with the Gatan ABF detector behaves similarly to the other samples, the Gatan HAADF detector shows a very distinct peak at ≈ 100 slices. Upon closer inspection this increase of intensity ratio is also visible for the other samples, albeit not as striking. When comparing corresponding detector images one can see, that the maximum intensity of the images increases up until 50 slices, where it begins to decrease up until ≈ 100 slices. At this point an increase sets in again. Since the delimiting factor for contrast magnitude are the Al columns, one should expect them to increase and decrease in intensity up to the denoted thickness values, which would have the impact in intensity ratio seen in figure 32

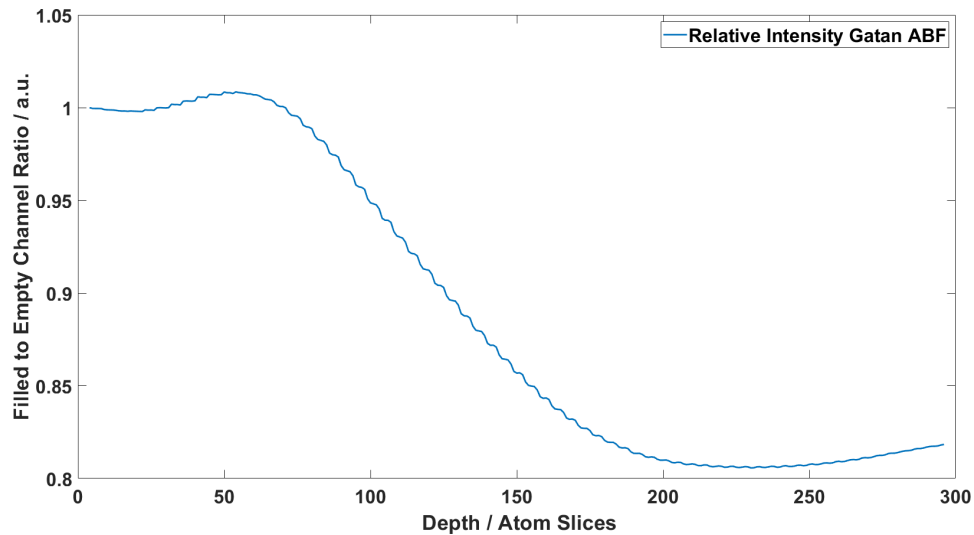
6.5 ^{66}Na -Dopants

As seen in figure 23 on page 31 the dopant atom peaks are very clearly visible across the whole crystal. The peak magnitude decreases with increasing crystal thickness, since the increase in dopant atoms has less impact on detected intensity values.

Due to the increase of dopant atoms across the whole crystal the intensity curve has a less steep decrease than other samples and a very smooth progression for increasing thickness.



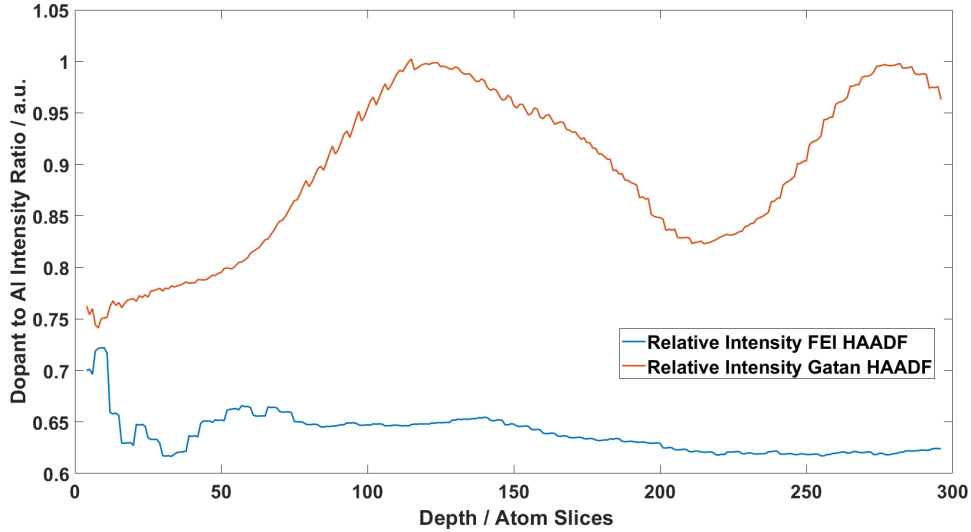
(a) FEI and Gatan HAADF intensity ratio of ^{66}Na to channel intensity. One atom slice is equal to 1.022 \AA .



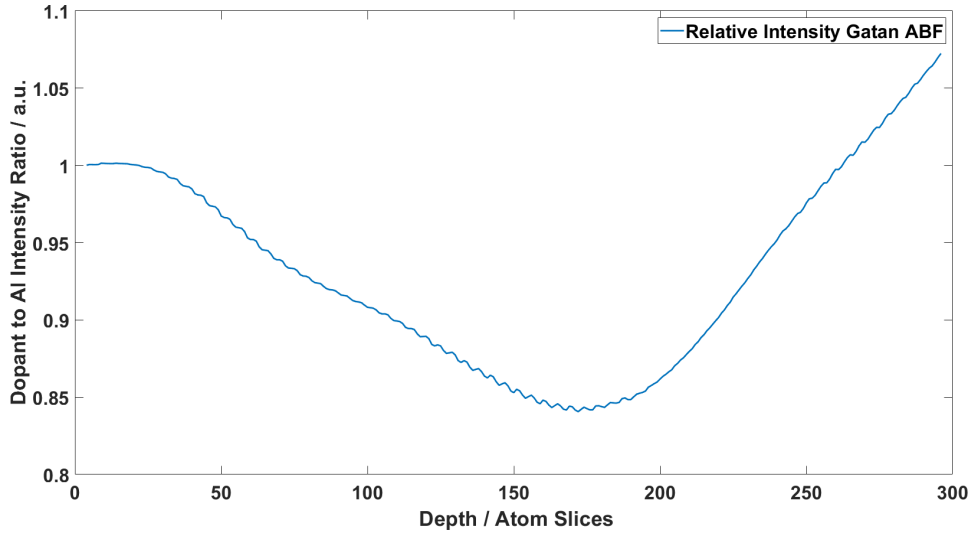
(b) Gatan ABF intensity ratio of ^{66}Na to channel intensity.

Figure 33: Ratio of integral results between the dopant column and channel intensity as a function of crystal slices. One atom slice is equal to 1.022 \AA .

The increasing dominance of the Na atom column compared to the empty channel intensity is very apparent in figure 33. Even at $t = 30 \text{ nm}$ the dopant is still clearly visible in the images, but also in the intensity data.



(a) FEI and Gatan HAADF intensity ratio of ^{66}Na to Al intensity. One atom slice is equal to 1.022 \AA .



(b) Gatan ABF intensity ratio of ^{66}Na to Al intensity.

Figure 34: Ratio of integral results between the dopant column and Al intensity as a function of crystal slices. One atom slice is equal to 1.022 \AA .

The FEI HAADF image in figure 34 behaves exactly as expected. Since the Na atoms are added in the crystal at the same height as the Al atoms, one should expect them to have similar intensity values across the whole crystal, which indeed they have. Their only difference is their intensity magnitude, which is apparent through their intensity ratio, which is ≈ 0.7 . This is expected as well, since Al is heavier than Na and scatters more in the high angle regime.

The Gatan HAADF image shows again a prominent peak at ≈ 120 slices, and an intensity increase due to channel contrast at ≈ 250 slices.

The Gatan ABF image implies more scattering for Al at lower thicknesses, with increasing scattering for Na at higher thicknesses. The turning point is positioned at ≈ 170 slices.

7 Evaluating Experimental Data

The simulation results from section 6 are used to determine the channel occupants from real HAADF images. Filled channels within the images are marked with red circles and numbered for reference purposes.

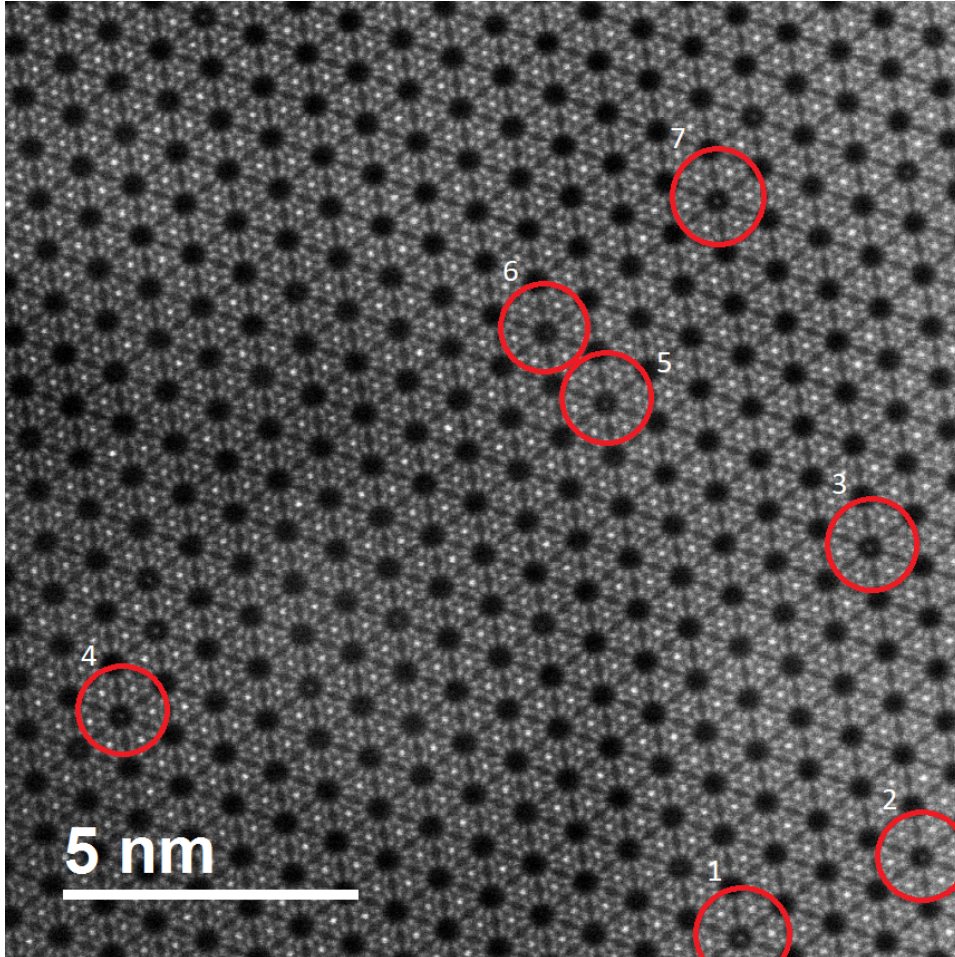


Figure 35: FEI HAADF image of bluegreen aquamarine, Christian Gspan (February 2015). Filled channels are marked with red circles.

The channels marked in figure 35 show the dopants that are integrated over. The following results show the ratios of the integrated dopant intensity and their surrounding channel intensity. In order to obtain good results the choice of position was made by dopant prominence and overall homogeneity of intensity in the dopant area.

Notice however, that a background subtraction must be performed first, otherwise the intensity ratio would be unreliable. To obtain the correct background intensity another image with a vacuum region was used for each detector, where the vacuum region served as background data.

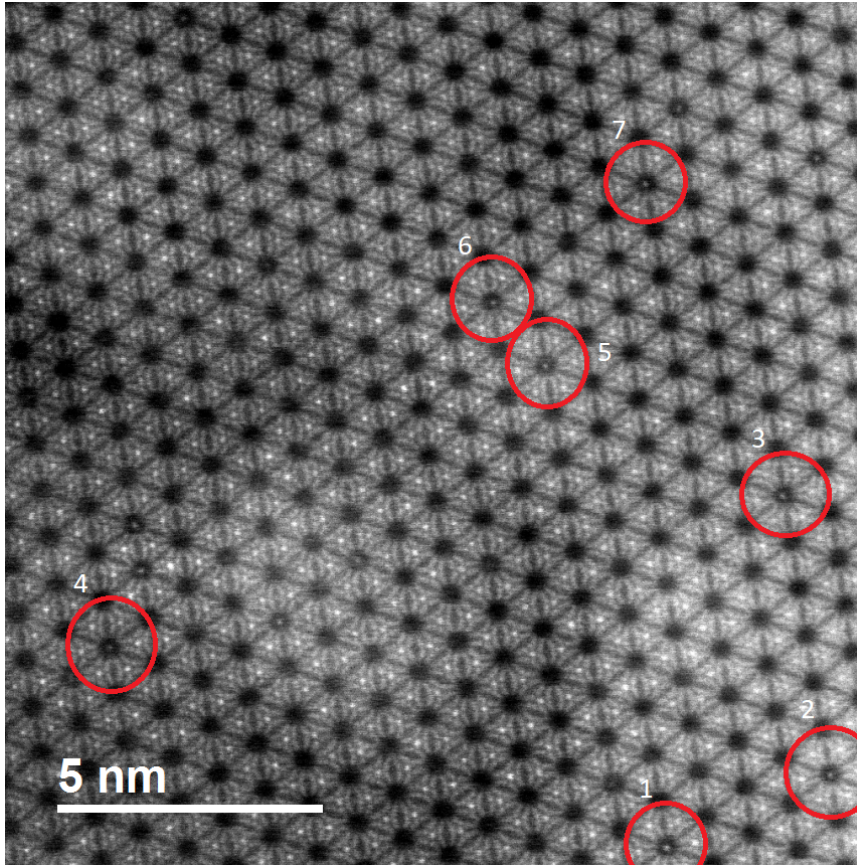
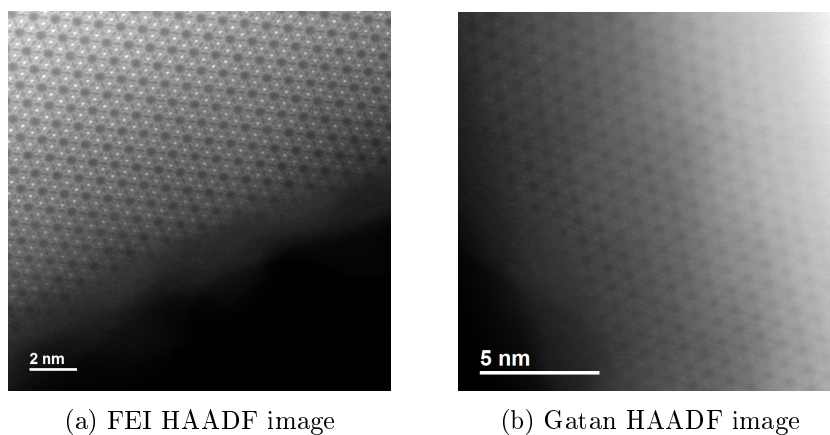


Figure 36: Gatan HAADF image of bluegreen aquamarine, Christian Gspan (February 2015). Filled channels are marked with red circles.

The dopants chosen for the Gatan image in figure 36 are the same as for the FEI image for comparison purposes.



(a) FEI HAADF image

(b) Gatan HAADF image

Figure 37: Images used for background calibration. Christian Gspan (February 2015 / May 2016).

The mean background intensity was determined by integrating over the vacuum areas and dividing by the integration area.

The software Seek & Integrate was used to calculate the integrals. The integrated intensities are shown in figures 38 and 39. Note that the images shown are rotated compared to the original detector images in figures 35 and 36.

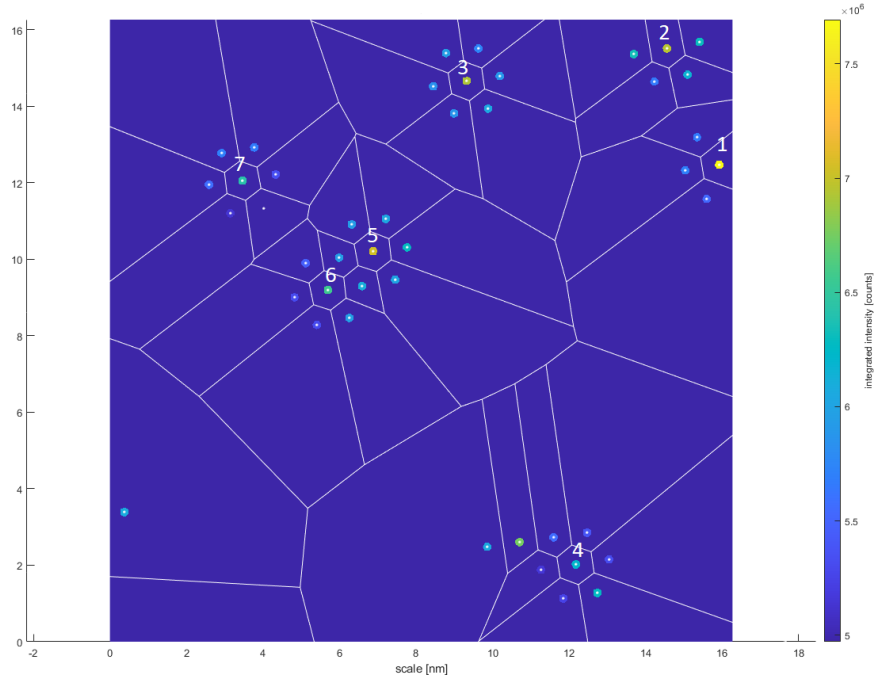


Figure 38: Integrated dopant and channel intensities for the FEI HAADF image.

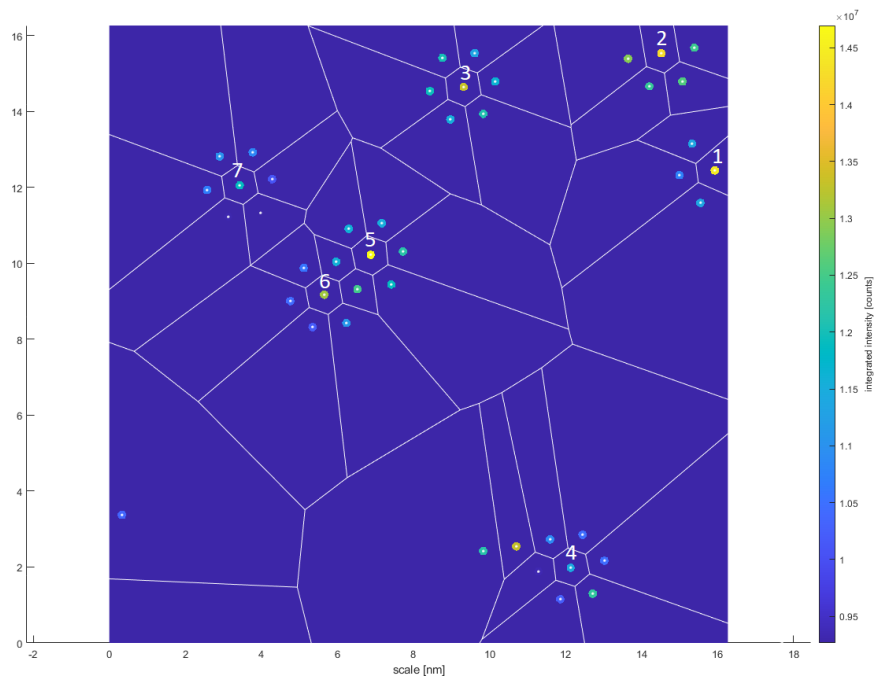


Figure 39: Integrated dopant and channel intensities for the Gatan HAADF image.

Table 7 shows the ratios of the dopant to channel intensities for the FEI HAADF and the Gatan HAADF images.

Ratio #	FEI HAADF	Gatan HAADF
1	1.36	1.30
2	1.14	1.13
3	1.17	1.13
4	1.13	1.08
5	1.16	1.13
6	1.15	1.18
7	1.19	1.16

Comparing the results from table 7 with simulation results one can see that certain positions are close to the ratios of simulated atoms. The data is shown in comparison to the simulation results in figures 40 and 41, where a crystal thickness of 25 nm is assumed. Note that the real crystal thickness is between 20 nm and 30 nm, and varies locally across the sample.

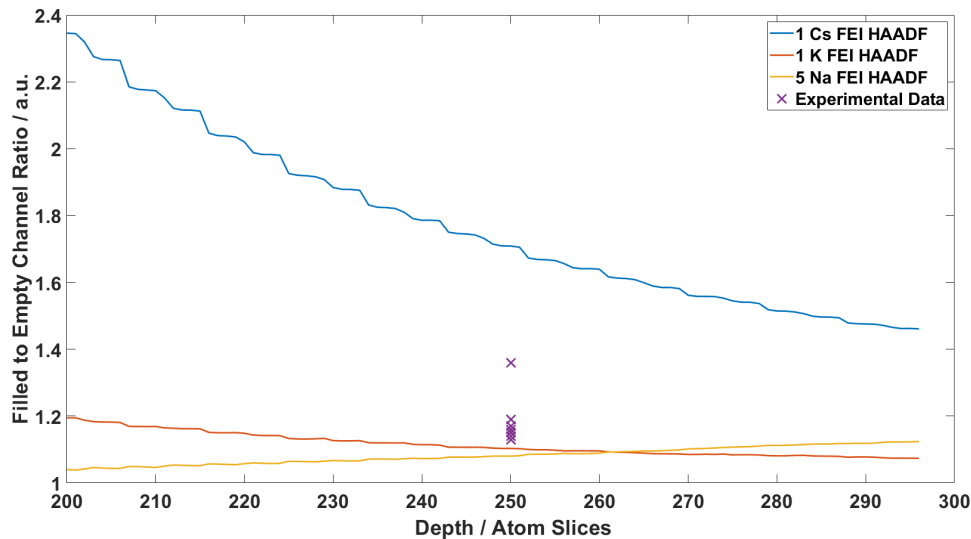


Figure 40: Ratio evaluation of experimental data for the FEI HAADF detector.

Figure 40 shows low spread for all values except for one, which is significantly higher than the others. This is an indication for a channel filled with a heavy atom like Cs or a large stack of atoms such as Na or K. Intensity ratios in this range were found in different crystal positions as well, which implies that this value is not merely a statistical outlier.

Most intensity ratios were in the range of 1.10 to 1.20, while brighter areas have a range of 1.30 to 1.40. This separation strongly hints at the presence Cs atoms, since Cs is the only atom with a high enough dopant- to channel intensity ratio to fit the simulation data. Other lighter elements such as K or stacks of Na all show lower ratios in the range of 1.10 to 1.20.

While the values are plotted at a thickness of 25 nm the real crystal has a thickness of 20 nm to 30 nm and varies locally.

The ratios obtained in table 7 are strongly dependent on subtracting the correct background intensity prior to integration, because the integrated dopant and channel intensities yield a different ratio when shifted by a constant value. Since this ratio is one of the main results obtained from the simulations, one ought to measure the background intensity in a vacuum area when performing STEM measurements for easier evaluation of experimental data. Therefore more experiments are required to further increase the reliability of the results.

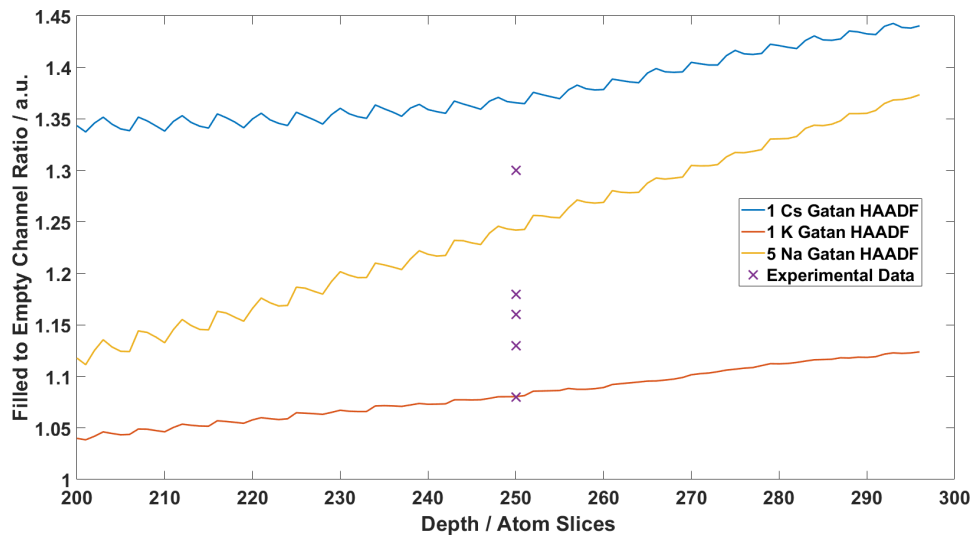


Figure 41: Ratio evaluation of experimental data for the Gatan HAADF detector.

The results for the Gatan HAADF detector are spread slightly less than the results of the FEI HAADF detector (note the different y-axis scaling in figures 40 and 41).

Note the data between the 1 K and 5 Na curve in figure 41. The spread between these two curves hints yet again at lighter elements such as Na and K, while the brighter spot is close to both the 1 Cs curve and the 5 Na curve.

This ambiguity would be resolved by measuring the vacuum intensity and measuring the crystal thickness as precisely as possible, as these parameters are most critical for this evaluation.

8 Summary

Documentation

The preparation for simulations and their proper execution were covered, with focus on required parameters and simulation replicability. All results are stored on the computing server of the FELMI-ZFE with their respective documentation and input data. Future simulations with different crystal sizes and dopants are performed easily by following the instructions in the documentation.

QSTEM Version Differences

While thermal diffusive scattering (TDS) is an important factor in simulations, choosing the correct amount of runs is paramount for efficient simulation performance. Please note that the results within this thesis have been obtained with QSTEM V2.4, while QSTEM V2.5 has a bug fix implemented, which corrects wrong temperature scaling from V2.4. By updating to QSTEM V2.5 future simulations could potentially lead to better intensity scaling and therefore to easier determination of channel contents in experimental measurements.

Importance of Dopant Positioning

One important note is that all simulations shown in this thesis were performed with the dopant atom on the topside of the crystal, since simulations with the dopant on the lower end of the crystal have shown no intensity at all at the filled channel. This was determined by comparing the integrated intensity of the filled channel with the surrounding empty channels, which has shown a ratio of 1. Future simulations with dopant atoms in the center of the crystal would shed more light on the position dependency of the dopant atom and could further improve experimental data evaluation.

Comparing Results by Eye and by Integration

The occupation of channels has been analyzed by intensity integration using the software package Seek & Integrate [21]. A comparison of dopant intensity integrals with integrals of their surrounding channels has shown that the channel atoms can be determined analytically with the use of simulation data. With enough experimental information such as background intensity and crystal thickness one can determine the channel occupants reliably. It is easy to mistake brighter spots within the channels for heavier atoms or for stacks of atoms, but one cannot tell by eye whether the surrounding channels are brighter as well. Therefore an analysis by integration is the only reliable way to determine channel contents theoretically.

The visibility of single dopant atoms like Cs or K is shown even for a crystal thickness of 30 nm. This shows that experiments on real beryl samples with thicknesses in the range of 30 nm may also be able to detect single atoms within the crystal channels. Lighter elements are not visible by eye but their presence can still be shown by integration.

Appendix

A MATLAB Code

Listing 1: Program for correcting .xyz file spacing.

```
1
2 %This program corrects the spacings from .xyz files given
3 % by VESTA and stores the corrected copy in another directory.
4
5 fileName = 'Beryl_66Na_6x6y33z.xyz'; %sample name
6
7 directory = 'C:\Users\Nikola\Documents\Masterarbeit\Sample ...
   Data\Self made defects\';
8
9 fid = fopen([directory fileName], 'r');
10
11 res={};
12 while ~feof(fid)
13     storage = fgetl(fid);
14     if ~ischar(storage); break; end
15     res{end+1,1} = storage;
16 end
17
18 numLines=numel(res);
19
20 dataLines = res;
21 for index = 1:numLines
22     if strcmp(dataLines{index}(1,1), ' ')
23         dataLines{index}(1,1:2) = [dataLines{index}(2), ' '];
24     end
25 end
26 fclose(fid);
27
28 writecell(dataLines, ...
   ['C:\Users\Nikola\Documents\Masterarbeit\Sample Data\Self ...
   made defects\Flipped ...
   Dopands\Corrected\'], fileName(1:end-4), 'Corrected.txt')
29
30 originalFileName = [fileName(1:end-4), 'Corrected.txt'];
31 newFileName = strrep(originalFileName, '.txt', '.xyz');
32
33 cd([directory, 'Flipped Dopands\Corrected'])
34
35 copyfile(originalFileName, newFileName);
36
37 cd('C:\Users\Nikola\Documents\Masterarbeit')
```

Listing 2: Program for evaluation of integration results and image acquisition.

```

1
2 %This program evaluates integral results for dopant atoms and Al
3 %intensities / empty crystal channels.
4 %The integral data is stored as .txt file to save execution
5 %time for future runs of the code. An automated fitting routine
6 %is included as well, where the fit function is choosable
7 %arbitrarily. Automated image acquisition from .img files is
8 %included aswell, where .img files are read, cropped and stored
9 %as .png files, which are readable more easily.
10
11 numberOfSlices = 99;%297; % 99 for z = 11 or 297 for z=33
12
13 compareToAl = true;
14 compareLeftRight = true;
15 doFits = false;
16
17 intensityPosition = 6;% 6 in regular cases
18
19 if compareToAl
20
21     dopantPosition = 9;    %#ok<*UNRCH>
22     xPlotSeparator = 50;
23     intensitiesFileName = 'intensities.txt';
24     detectorNameExtension = '_maxLocations_results.xls';
25     plotYLabel = 'Dopant to Al Intensity Ratio / a.u.';
26
27
28 else
29
30     dopantPosition = 4;
31     xPlotSeparator = 50;
32     intensitiesFileName = 'intensitiesHoles.txt';
33     detectorNameExtension = '_maxLocationsHoles_results.xls';
34     plotYLabel = 'Filled to Empty Channel Ratio / a.u.';
35
36 end
37
38
39
40 if ~exist(intensitiesFileName, 'file')
41     tic
42
43
44     folderContents = struct2cell(dir);
45     folderContents = folderContents(1,:);
46
47     relevantFileNames = cell(size(folderContents,2),1);
48     fileCounter = 0;
49
50     for k = 1:size(folderContents,2)
51         try
52             if strcmp(folderContents{k}(end-2:end), 'xls')
53
54                 relevantFileNames{k} = folderContents{k};
55                 fileCounter = fileCounter + 1;
56
57             end
58
59

```

```
60     catch
61
62     end
63 end
64
65 relevantFileNames = relevantFileNames(~cellfun('isempty', ...
        relevantFileNames));
66
67 %%%%%%%%%SET NUMBER OF UNIT CELLS
68 Z = fileCounter /10 / 9;
69
70 sortedFileNames = cell(fileCounter,1);
71
72 numberOfSlices = size(relevantFileNames,1) / 10;
73 %sample file name: 'detector1_37_maxLocations_results.xls'
74
75 subCounter = 0;
76 detectorCount = 1;
77
78 for k = 1:fileCounter
79
80     sortedFileNames{k} = ['detector', ...
            num2str(detectorCount), '_', num2str(subCounter), ...
            detectorNameExtension ];
81
82     if subCounter == (numberOfSlices - 1)
83
84         subCounter = 0;
85         detectorCount = detectorCount + 1;
86
87     else
88
89         subCounter = subCounter + 1;
90
91     end
92
93 end
94
95 for k = 1:fileCounter
96
97     M = table2array(readtable(sortedFileNames{k}));
98
99     if k == 1
100         intensities = zeros(size(M,1),fileCounter);
101     end
102
103     intensities(:,k) = M(:,intensityPosition);
104
105 end
106
107 writematrix(intensities, intensitiesFileName)
108
109 toc
110
111 end
112
113 if exist(intensitiesFileName, 'file')
114     intensities = load(intensitiesFileName);
115 end
116
117 referenceIntensities = intensities;
118 referenceIntensities(dopantPosition,:) = [];
```

```

119 referenceIntensities = mean(referenceIntensities);
120
121 %k goes from detector 1 to detector 10, or from 0 to 9
122 coeff = zeros(3,10);
123 coeffShorterZ = zeros(2,10);
124
125 formFunction = @(beta, t) beta(2)*exp(-t/beta(1)) + beta(3);
126
127 formFunctionAlternative = @(beta, t) beta(2)*exp(-t/beta(1));
128
129
130
131 for k = 0:2%9
132
133     if k == 0 || k == 2
134         figure(k+1)
135     end
136     relativeIntensity = ...
137         intensities(dopantPosition, ((k*numberOfSlices + ...
138             1):(k*numberOfSlices + numberOfSlices)))...
139         ./referenceIntensities(((k*numberOfSlices + ...
140             1):(k*numberOfSlices + numberOfSlices)));
141
142     %Full Z length fit
143     if k ≠ 2 && k≠7
144         if doFits
145             coeff(:, k+1) = nlinfit(4:numberOfSlices-1, ...
146                 relativeIntensity(5:end), ...
147                 formFunction, [1,100,0.1]);
148         end
149         if compareLeftRight
150
151             yDataLeft = relativeIntensity(5:xPlotSeparator);
152             yDataRight = relativeIntensity(xPlotSeparator:end);
153
154             yyaxis left
155             plot( 4:xPlotSeparator-1, yDataLeft, 'LineWidth', 2 )
156             ylim([0, max(yDataLeft)])
157             xlabel(' Depth / Atom Slices', 'FontSize', 24)
158             ylabel(plotYLabel, 'FontSize', 24)
159             a = get(gca, 'XTickLabel');
160             set(gca, 'fontsize', 24, 'FontWeight', 'bold')
161
162             yyaxis right
163             plot( xPlotSeparator:numberOfSlices, yDataRight, ...
164                 'LineWidth', 2)
165             ylim([0, max(yDataRight)])
166             hold on
167
168         else
169
170             plot( 4:numberOfSlices-1, ...
171                 relativeIntensity(5:end), 'LineWidth', 2 )
172             hold on
173         end
174     elseif k ==2
175
176         hold off
177         plot( 4:numberOfSlices-1, relativeIntensity(5:end), ...

```

```

        'LineWidth', 2 )
174
175     end
176     xlabel(' Depth / Atom Slices', 'FontSize', 24)
177     ylabel(plotYLabel, 'FontSize', 24)
178     a = get(gca, 'XTickLabel');
179     set(gca, 'fontsize', 24, 'FontWeight', 'bold')
180     if k == 0 || k == 1
181         legend('Relative Intensity FEI HAADF', 'Relative ...
                Intensity Gatan HAADF', 'FontSize', 24, ...
                'Location', 'southeast')
182     else
183         legend('Relative Intensity Gatan ABF', 'FontSize', 24)
184     end
185     %Lower Z length fit
186     difference = numberOfSlices - 9 ;
187     if doFits
188         coeffShorterZ(:, k+1) = ...
            nlinfit(0:numberOfSlices-difference, ...
                relativeIntensity(1:(numberOfSlices-difference + ...
                    1)), formFunctionAlternative, [1,100]);
189     end
190
191     if doFits
192         if ~exist('coeffs.txt', 'file') && k==9
193             writematrix(coeff, 'coeffs.txt')
194         end
195     end
196
197     if doFits
198         if ~exist('coeffsShorterZDepth.txt', 'file') && k==9
199             writematrix(coeffShorterZ, 'coeffsShorterZDepth.txt')
200         end
201     end
202
203 end
204
205 %Read DetectorData
206 %
207 % for detectorIndex = 1:3
208 %     for k = 1:9
209 %         directory = 'D:\';
210 %         numbers = {296};%{0,9,18,27,45,99,135,180,296};
211 %         number = num2str(numbers{k});
212 %
213 %         file = ['detector', num2str(detectorIndex), '_', ...
                number, '.png'];
214 %
215 %         picture = imread([directory, file]);
216 %         picture = picture(20:464, 20:460, :);
217 %         figure
218 %         imshow(picture, [min(picture(:)), max(picture(:))])
219 %         imwrite(picture, [directory, file])
220 %         close all
221 %     end
222 % end

```

References

- [1] W. L. BRAGG, J. WEST. *The structure of beryl, $Al_2Be_3[Si_6O_{18}]$* . Proceedings of the Royal Society of London. Series A, Containing Papers of a Mathematical and Physical Character **111** (1926) 691.
doi:10.1098/rspa.1926.0088
- [2] C. AURISICCHIO, G. FIORAVANTI, O. GRUBESSI, P. F. ZANAZZI. *Reappraisal of the crystal chemistry of beryl*. American Mineralogist **73** (1988) 826.
- [3] B. P. GORSHUNOV, *et al.* *Incipient ferroelectricity of water molecules confined to nano-channels of beryl*. Nat. Commun. 7:12842 doi: 10.1038/ncomms12842. (2016).
- [4] A. I. KOLESNIKOV, G. F. REITER, N. CHOUDHURY, T. R. PRISK, E. MAMONTOV, A. PODLESNYAK, G. EHLERS, A. G. SEEL, D. J. WESOŁOWSKI, L. M. ANOVITZ. *Quantum Tunneling of Water in Beryl: A New State of the Water Molecule*. Phys. Rev. Lett. **116** (2016) 167802.
doi:10.1103/PhysRevLett.116.167802
- [5] F. HOFER. Non published results with TEM Philips CM20, 1990.
- [6] C. GSPAN, F. HOFER. non published ASTEM results, refer to FELMI-ZFE performance report 2012-2014, Graz University of Technology, 2015.
- [7] V. ARIVAZHAGAN, F. SCHMITZ, P. VULLUM, A. VAN HELVOORT, B. HOLST. *Atomic resolution imaging of beryl: an investigation of the nano-channel occupation*. Journal of Microscopy **265** (2017) 245.
doi:https://doi.org/10.1111/jmi.12493
- [8] FELMI-ZFE Performance Report 2009-2011, Graz University of Technology (2012) 38-40. .
- [9] C. T. KOCH, QSTEM: Quantitative TEM/STEM Simulations. [Online; visited October-2020].
https://www.physics.hu-berlin.de/en/sem/software/software_qstem
- [10] V. ARIVAZHAGAN, F. SCHMITZ, P. VULLUM, A. VAN HELVOORT, B. HOLST. *Atomic resolution imaging of beryl: an investigation of the nano-channel occupation*. Journal of Microscopy **265** (2017) 245.
doi:10.1111/jmi.12493
- [11] C. T. KOCH. *Determination of core structure periodicity and point defect density along dislocations*. Arizona State University, doctoral dissertation (2002).
- [12] M. QUIRÓS, S. GRAŽULIS, S. GIRDIJIAUSKAITĖ, A. MERKYS, A. VAITKUS. *Using SMILES strings for the description of chemical connectivity in the Crystallography Open Database*. Journal of Chemin-

- formatics **10** (2018).
doi:10.1186/s13321-018-0279-6
- [13] A. MERKYS, A. VAITKUS, J. BUTKUS, M. OKULIČ-KAZARINAS, V. KAIRYS, S. GRAŽULIS. *COD::CIF::Parser: an error-correcting CIF parser for the Perl language*. Journal of Applied Crystallography **49** (2016).
doi:10.1107/S1600576715022396
- [14] S. GRAŽULIS, A. MERKYS, A. VAITKUS, M. OKULIČ-KAZARINAS. *Computing stoichiometric molecular composition from crystal structures*. Journal of Applied Crystallography **48** (2015) 85.
doi:10.1107/S1600576714025904
- [15] S. GRAŽULIS, A. DAŠKEVIČ, A. MERKYS, D. CHATEIGNER, L. LUTTEROTTI, M. QUIRÓS, N. R. SEREBRYANAYA, P. MOECK, R. T. DOWNS, A. LE BAIL. *Crystallography Open Database (COD): an open-access collection of crystal structures and platform for world-wide collaboration*. Nucleic Acids Research **40** (2012) D420.
doi:10.1093/nar/gkr900
- [16] S. GRAŽULIS, D. CHATEIGNER, R. T. DOWNS, A. F. T. YOKOCHI, M. QUIRÓS, L. LUTTEROTTI, E. MANAKOVA, J. BUTKUS, P. MOECK, A. LE BAIL. *Crystallography Open Database – an open-access collection of crystal structures*. Journal of Applied Crystallography **42** (2009) 726.
doi:10.1107/S0021889809016690
- [17] R. T. DOWNS, M. HALL-WALLACE. *The American Mineralogist Crystal Structure Database*. American Mineralogist **88** (2003) 247.
- [18] K. MOMMA, F. IZUMI. *VESTA3 for three-dimensional visualization of crystal, volumetric and morphology data*. Journal of Applied Crystallography **44** (2011) 1272.
doi:10.1107/S0021889811038970
- [19] C. GSPAN, W. GROGGER, F. HOFER. *Unpublished Results* (2015-2016).
- [20] D. KNEZ. *Scanning transmission electron microscopy of metallic clusters and nanoalloys*. Dissertation, Graz University of Technology, Graz, 2017.
<https://graz.pure.elsevier.com/de/publications/scanning-transmission-electron-microscopy-of-metallic-clusters-an>
- [21] D. KNEZ, G. DRAŽIĆ, S. K. CHALUVADI, P. ORGIANI, S. FABRIS, G. PANACCIONE, G. ROSSI, R. CIANCIO. *Unveiling Oxygen Vacancy Superstructures in Reduced Anatase Thin Films*. Nano letters **20** (2020) 6444.
doi:10.1021/acs.nanolett.0c02125
- [22] L. JONES, K. E. MACARTHUR, V. T. FAUSKE, VAN HELVOORT, ANTONIUS T J, P. D. NELLIST. *Rapid estimation of catalyst nanoparticle morphology and atomic-coordination by high-resolution Z-contrast electron microscopy*. Nano letters **14** (2014) 6336.
doi:10.1021/nl502762m